



1 **Visibility-derived aerosol optical depth over global land from 1980 to** 2 **2021**

3 Hongfei Hao¹, Kaicun Wang², Chuanfeng Zhao³, Guocan Wu¹, Jing Li³

4 ¹Global Change and Earth System Science, Faculty of Geographical Science, Beijing Normal
5 University, Beijing 100875, China

6 ²Institute of Carbon Neutrality, Sino French Institute of Earth System Science, College Urban and
7 Environmental Sciences, Peking University, Beijing 100871, China

8 ³Institute of Carbon Neutrality, Department of Atmospheric and Oceanic Sciences, School of
9 Physics, College Urban and Environmental Sciences, Peking University, Beijing 100871, China

10

11 Corresponding Author: Kaicun Wang, Email: kewang@pku.edu.cn

12

13 **Abstract**

14 Long-term and high spatial resolution aerosol optical depth (AOD) data are necessary for climate
15 change detection and attribution. Global ground-based AOD observation stations are sparse, and
16 satellite AOD observations have a low time frequency, as well low accuracy before 2000. In this
17 study, AOD was derived from hourly visibility observations collected at more than 5000 stations of
18 the Automated Surface Observing System (ASOS) over global land from 1980 to 2021. The AOD
19 retrievals of the Moderate Resolution Imaging Spectroradiometer (MODIS) onboard the Aqua Earth
20 observation satellite were used to train the machine learning method, and the ERA5 reanalysis
21 boundary layer height was used as input. The predicted result has correlation coefficients of 0.54
22 and 0.51 with Terra MODIS satellite retrievals and AERONET ground observations. The correlation
23 coefficients are higher at monthly and annual scales, which are 0.81 and 0.61 for the monthly and
24 0.91 and 0.62 for the annual, when compared with Terra MODIS and AERONET AOD, respectively.
25 The visibility-derived AOD at ASOS stations was gridded into a 0.5-degree resolution by area-
26 weighted ordinary kriging interpolation. Analysis of visibility-derived AOD indicates that the global
27 mean AOD over land is 0.16, which is 0.24, 0.22, 0.11, 0.11, 0.130, and 0.12 for Africa, Asia, Europe,
28 North America, Oceania, and South America, respectively. The mean AOD over global land, the
29 Northern Hemisphere, and the Southern Hemisphere demonstrated decreasing trends of -0.0026/10a,
30 -0.0018/10a, and -0.0059/10a, respectively, from 1980 to 2021. The visibility-derived AOD at
31 station and grid scales over global land from 1980 to 2021 are available at National Tibetan Plateau
32 / Third Pole Environment Data Center (<https://doi.org/10.11888/Atmos.tpdc.300822>) (Hao et al.,
33 2023).

34 How to cite. Hao, H., Wang, K., C. Zhao, Wu, G., J. Li (2023). Visibility-derived aerosol optical
35 depth over global land (1980-2021). National Tibetan Plateau / Third Pole Environment Data
36 Center. <https://doi.org/10.11888/Atmos.tpdc.300822>.



37 1 Introduction

38 Atmospheric aerosols are composed of solid and liquid particles suspended in the atmosphere.
39 Aerosol particles are primarily discharged from the Earth's surface broadly classified into natural
40 and anthropogenic sources (Calvo et al., 2013). They possess diverse shapes and sizes (Fan et al.,
41 2021), optical properties, and various components (Li et al., 2022), such as inorganic salts, organic
42 matter, metal elements and elemental carbon. Most atmospheric aerosols are concentrated in the
43 troposphere, especially in the boundary layer (Liu et al., 2022), with a high concentration near
44 emission sources (Kulmala et al., 2004), and a small portion are distributed in the stratosphere with
45 a sharp increase during large volcanic eruptions. Some aerosols from wildfires, volcanoes and
46 sandstorms, play an important role in tropospheric aerosols. Studies have showed that 75% of
47 volcanic eruptions inject volcanic aerosols and sulfur containing gases into the troposphere (Halmer
48 et al., 2002), wildfire aerosols contribute up to approximately 35% of the fine particles in Europe
49 (Barnaba et al., 2011), and dust aerosols are mainly concentrated in the middle and low troposphere
50 (Filonchik et al., 2018). Atmospheric aerosols severely impact the atmospheric environment and
51 human health. They deteriorate air quality, reduce visibility, and cause other environmental issues
52 (Wang et al., 2012; Boers et al., 2015). They affect human health or other organisms' conditions by
53 increasing cardiovascular and respiratory disease incidence and mortality rates (Chafe et al., 2014;
54 Yang et al., 2022). The Global Burden of Disease shows that global exposure to ambient PM_{2.5}
55 resulted in 0.37 million deaths and 9.9 million disability-adjusted life years (Chafe et al., 2014).

56 In addition to environmental and health impacts, aerosols are inextricably linked to climate change.
57 Atmospheric aerosols alter the Earth's energy budget and then affect the climate (Li et al., 2022).
58 They cool the surface and heat the atmosphere by scattering and absorbing solar radiation (Forster
59 et al., 2007; Chen et al., 2022). Aerosols, such as black carbon and brown carbon, also absorb solar
60 radiation (Bergstrom et al., 2007), heat the local atmosphere and suppress or invigorate convective
61 activities (Ramanathan et al., 2001; Sun & Zhao, 2020). Aerosols also alter the optical properties
62 and life span of clouds (Albrecht, 1989). Atmospheric aerosols strongly affect regional and global
63 short-term and long-term climates through direct and indirect effects (McNeill, 2017).

64 Tropospheric aerosols are considered as the second largest forcing factor for global climate change
65 (Li et al., 2022), and they reduce the warming due to greenhouse gases by -0.5°C (IPCC, 2021).
66 However, aerosols are also regarded as the largest contributor to quantifying the uncertainty of
67 present-day climate change (IPCC, 2021). The deficiency of the global descriptions of aerosol
68 optical and microphysical properties is the primary reason for the uncertainty and the uncertainty
69 also exists in climate models (Lee et al., 2016; IPCC, 2021). Therefore, sufficient aerosol
70 observations are crucial. In aerosol measurements, aerosol optical depth (AOD) is often used to
71 describe its column properties, which represents the vertical integration of aerosol extinction
72 coefficients. AOD is an important physical quantity for estimating the content, atmospheric
73 pollution and climatology of aerosols (Zhang et al., 2020).

74 The measurements of aerosols are usually divided into in-situ and remote sensing observations. In-
75 situ observations accurately measure the mass, number concentration, shapes, compositions and
76 scattering and absorption of aerosols by directly sampling the air (Herich et al., 2008; Laj et al.,
77 2020). Observations from airplanes and balloons can provide vertical structure (Ziemba et al., 2013).



78 Because of its accuracy, in-situ observation is often used as the benchmark for models and satellites,
79 but its spatial representativeness is limited. Another method is ground-based lidar observation,
80 which is an active remote sensing technology. Lidar generally emits laser and receives backscattered
81 signals to invert the extinction coefficient of aerosols at different heights (Klett, 1985). By using the
82 depolarization ratio, the type of aerosol, such as fine particles or dust, can also be distinguished
83 (Bescond et al., 2013). The AOD within a certain height can be calculated by integrating the
84 extinction coefficients; however, scattering signals are usually not received near the ground, leading
85 to blind spots (Singh et al., 2019). At present, there are many ground-based lidar worldwide and
86 regional networks, which provides important support in the study of vertical changes in aerosols,
87 such as the NASA Micro-Pulse Lidar Network (MPLNET) in the early 1990s (Welton et al., 2002),
88 the European Aerosol Research Lidar Network (EARLINET) since 2000 (Bösenberg & Matthias,
89 2003), the Latin American Lidar Network (LALINET) since 2013 (Guerrero-Rascado et al., 2016).

90 The other two passive remote sensing observations of aerosol properties are ground-based and
91 satellite-borne remote sensing observations. Ground-based remote sensing observations supply
92 aerosol loading data (such as AOD), by measuring the attenuation of radiation from the top of the
93 atmosphere to the surface (Holben et al., 1998). This type of observations mainly uses weather-
94 resistant automatic sun and sky scanning spectral radiometers to retrieve optical and microphysical
95 aerosol properties (Che et al., 2014). The Aerosol Robotic Network (AERONET) is a popular global
96 network composed of NASA and multiple international partners that provides high-quality and high-
97 frequency aerosol optical and microphysical properties under various geographical and
98 environmental conditions (Holben et al., 1998; Dubovik et al., 2000). The AERONET observations
99 are extensively used to validate of satellite remote sensing observations and model simulations, as
100 well as climatology study (Dubovik et al., 2002b). There are many regional networks of sun
101 photometers, such as the Maritime Aerosol Network (MAN), which use a handheld sun photometer
102 to collect data on the ocean and is merged into AERONET (Smirnov et al., 2009), the China Aerosol
103 Robot Sun Photometer Network(CARSNET) (Che et al., 2009), the Canadian sub-network of
104 AERONET (AEROCAN) (Bokoye et al., 2001), Aerosol characterization via Sun photometry:
105 Australian Network (AeroSpan) (Mukkavilli et al., 2019), and the sky radiometer network
106 (SKYNET) in Asia and Europe (Kim et al., 2004; Nakajima et al., 2020). Another very valuable
107 global network is the NOAA/ESRL Federated Aerosol Network (FAN), which uses integrated
108 nephelometers distinct from sun photometers, mainly located in areas with less human activity
109 impact, providing regionally representative aerosol properties over 30 sites (Andrews et al., 2019).

110 Satellite remote-sensing is a space-based method that can provide aerosol properties worldwide.
111 With the development of satellite remote sensing technology since 1970, aerosol distributions can
112 be extracted with the advantage of sufficient real-time and global coverage from multiple satellite
113 sensors (Kaufman & Boucher, 2002; Anderson et al., 2005). The Advanced Very High Resolution
114 Radiometer (AVHRR) was the earliest sensor used for retrieving AOD over ocean (Nagaraja Rao et
115 al., 1989). The Moderate Resolution Imaging Spectroradiometer (MODIS), on board the Terra
116 (launched in 1999) and Aqua (launched in 2002) satellites is a popular sensor with 36 channels,
117 which have been used for AOD retrieval over both ocean and land based on the Dark Target and the
118 Deep Blue algorithms (Remer et al., 2005; Levy et al., 2013). The latest MODIS AOD data version
119 is the Collection 6.1, which provides global AOD over 20 years (Wei et al., 2019a). There are also
120 many other satellite sensors that can be used to retrieve AOD, such as the Polarization and



121 Directionality of the Earth's Reflectances (POLDER) during 1996-1997, 2003 and 2004-2013
122 (Deuzé et al., 2000), Sea-viewing Wide Field-of-view Sensor (SeaWiFS) during 1997-2007
123 (O'Reilly et al., 1998), the Multi-angle Imaging Spectroradiometer (MISR) on Terra since 1999
124 (Diner et al., 1998). The Cloud-Aerosol Lidar with Orthogonal Polarization (CALIOP) has also
125 derived aerosols in the vertical direction since 2006 (Winker et al., 2009).

126 These measurements provide important data for studying the global and regional spatiotemporal
127 variabilities and climate effect of aerosols. However, in-situ and ground-based remote sensing
128 observations only provide aerosol properties with low spatial coverage. There were only 1126
129 ground stations worldwide in 2002 and even fewer sites were available for climate analysis (Holben
130 et al., 1998; Chu et al., 2002), which limited aerosol climate research by spatial coverage (Bright &
131 Gueymard, 2019). Satellite remote sensing overcomes the limitations of spatial coverage. The
132 AVHRR has been used to retrieve AOD since 1980, but it is limited by a few channel number, low
133 spatial resolution, and insufficient validation through ground-based observations before 2000 (Hsu
134 et al., 2017). Many studies have only investigated the trends and distributions of aerosols after 2000
135 (Bösenberg & Matthias, 2003; Winker et al., 2013; Xia et al., 2016; Tian et al., 2023), because of
136 the lack of long-term and global cover AOD products, which is the bottleneck for aerosol climate
137 change detection and attributions.

138 To overcome these limitations and enrich aerosol data, alternative observation data could be utilized
139 to derive AOD. For example, some studies used solar radiation data to infer AOD and analyze the
140 characteristics of AOD in different regions (King et al., 1978; Vasilyev et al., 1995; Marengo et al.,
141 1997; Qiu, 1997). There are also some studies deriving AOD based on empirical relationship
142 between particle concentration and AOD (Xie et al., 2015; Li, 2020). These methods partially
143 mitigate the scarcity of AOD data in spatial coverage, but it is also important to acknowledge the
144 inherent limitation of long temporal coverage. Another more suitable alternative is atmospheric
145 horizontal visibility, because it has the advantages of the long-term records with a large number of
146 stations worldwide.

147 Atmospheric visibility is a physical quantity that describes the transparency of the atmosphere
148 through manual and automatic observations. The automatic observations of visibility usually
149 measure atmospheric extinction (scattering coefficient and transmissivity), including particle matter,
150 water vapor, and gas molecules (Wang et al., 2009; Zhang et al., 2020), which makes it a favorable
151 choice for inferring AOD. Koschmieder (1924) first proposed the relationship between the
152 meteorological optical range and the total optical depth. Elterman (1970) further established a
153 formula between AOD and visibility by assuming an exponential decrease in aerosol concentration
154 with altitude, considering the extinction of molecules and ozone to analyze air pollution, which
155 called the Elterman model. Qiu and Lin (2001) corrected the Elterman model by considering the
156 influence of water vapor and used two water vapor pressure correction coefficients to retrieve AOD
157 of 16 stations in China in 1990. Lin et al. (2014) retrieved the AOD in eastern China in 2006 using
158 visibility and aerosol vertical profiles provided by GEOS-Chem. Wu et al. (2014) and Zhang et al.
159 (2017) parameterized the constants in the Elterman model and use satellite retrieved AOD to solve
160 the parameters in the models at different stations, to retrieve the long-term AOD in China. Zhang et
161 al. (2020) reviewed the methods of visibility retrieval of AOD, indicating that visibility-based
162 retrieval of AOD can compensate for the shortcomings of long-term aerosol observation data.
163 Simultaneously, various parameters, such as station altitude, consistency of visibility data, water



164 vapor and aerosol vertical profiles (scale height), were discussed with modified suggestions
165 proposed. These studies have enriched AOD data regionally. Due to the similar spatial distribution
166 of the extinction coefficient and AOD, and the proportional relationship between the reciprocal of
167 visibility and the extinction coefficient, Wang et al. (2009) analyzed the trend of AOD using
168 visibility-based retrievals from 1973 to 2007 over land. These studies have enriched aerosol data in
169 some extent. At present, there are very few studies on global visibility-retrieved AOD and to analyze
170 climatology of aerosols.

171 The two physical quantities of visibility and AOD have both connections and differences, making it
172 challenging to retrieve AOD from visibility. Visibility represents the maximum horizontal visible
173 distance near the surface, while AOD represents the total vertical attenuation of solar radiation by
174 aerosols. The visibility of automatic observation is dependent on the local horizontal atmospheric
175 extinction (NOAA et al., 1998). Visibility has not a simple linear relationship with meteorological
176 factors, such as humidity and wind speed. The vertical structure of aerosols is the greatest challenge
177 to obtain, as it is not a simple hypothetical curve in complex terrain and circulation conditions
178 (Zhang et al., 2020). These limitations make it more complex to derive AOD over global land.
179 However, previous studies have shown that surface observation data can establish a link with AOD,
180 particularly at the regional scale. Machine learning methods can effectively address complex
181 nonlinear relationships between variables and have been widely applied in remote sensing and
182 climate research fields. Li et al. (2021) used the random forest method to predict $PM_{2.5}$ in Iraq and
183 Kuwait based on satellite AOD during 2001-2018. Kang et al. (2022) applied LightGBM and
184 random forest to estimate AOD over East Asia, and the results showed a consistency with
185 AERONET. Dong et al. (2023) derived aerosol single scattering albedo from visibility and satellite
186 AOD over 1000 global stations. Hu et al. (2019) used a deep learning method to retrieve horizontal
187 visibility from MODIS AOD. These studies have confirmed the ability of machine learning to
188 effectively solve complex relationships among variables. Thus, it is feasible to derive AOD from
189 atmospheric visibility by using the machine learning method.

190 In this study, we propose a machine learning method to derive AOD, where satellite AOD is the
191 target value, and surface visibility and other related meteorological variables are the predictors. We
192 explain the robustness of the model, validate the accuracy of the model's predictions using ground-
193 based AOD and other observations, and analyze the climatology of AOD across land and regions.
194 Two datasets of long-term high-resolution AOD are generated. The second part of this paper
195 introduces the data and method. The third part is the evaluation and validation of the visibility-
196 derived AOD, and the distribution and trends are discussed at global and regional scales. The fourth
197 part presents the conclusions. This study is dedicated to supporting the research of aerosols in
198 climate change detection and attribution.

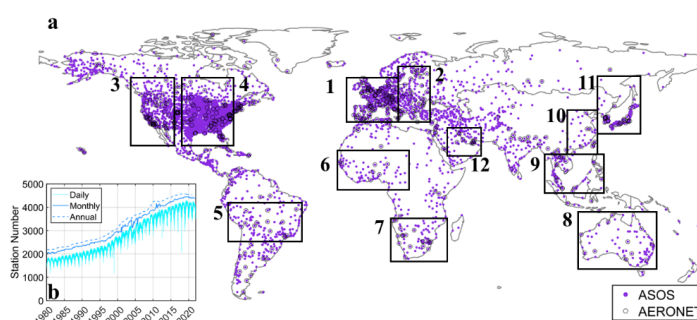
199 **2 Data and method**

200 **2.1 Study area**

201 The study area is global land region. A total of 5032 land stations of the Automated Surface
202 Observing System (ASOS), which is a joint surface weather observing network of the National
203 Weather Service (NWS), the Federal Aviation Administration (FAA), and the Department of
204 Defense (DOD) (NOAA et al., 1998). A total of 573 stations of AERONET are selected in this study



205 and shown in Figure 1 (a). 12 typical regions are selected for analysis, including Eastern Europe,
206 Western Europe, Western North America, Eastern North America, Central South America, Western
207 Africa, Southern Africa, Australia, Southeast Asia, Northeast Asia, Eastern China, and Middle East.
208 The time range in the study is from 1980 to 2021, during which the records of ASOS stations are
209 sufficient with a uniform spatial distribution. As shown in Figure 1 (b), the daily records have
210 exceeded 1500 stations, and monthly and annual records have exceeded 2000 during 1980-1990.
211 After 2000, monthly records have reached 3000, which is the foundation of gridding AOD.



212

213 **Figure 1** Study area (a) and the station number (b) with daily, monthly, and annual records in the
214 Automated Surface Observing System (ASOS). The number of ASOS stations (filled circles) is
215 5032. The number of AERONET stations (empty circles) is 573. The box regions of labelled with
216 number 1-12 are Eastern Europe, Western Europe, Western North America, Eastern North America,
217 Central South America, Western Africa, Southern Africa, Australia, Southeast Asia, Northeast Asia,
218 Eastern China, and Middle East.

219 2.2 Ground-based observations

220 Ground-based hourly observation data from 1980 to 2021 are collected at 5032 globally distributed
221 stations (Figure 1) from the ASOS program. From the 1960s to the 1970s, the Automated
222 Meteorological Observing System (AMOS) and Remote Automated Weather Observing System
223 (RAMOS) only reported objective elements, such as temperature, dew point temperature, wind
224 (speed and direction), and pressure. With technological advancements, the ASOS was deployed and
225 utilized in the 1980s. The automatic surface observations reduced errors associated with human
226 involvement in data acquisition, processing, and transmission. Effective quality control methods are
227 employed to ensure the quality of ASOS products. ASOS provided hourly and even minutely ground
228 automatic observations, primarily for airports (NOAA et al., 1998; Dover et al., 2002).

229 Atmospheric visibility from ASOS is measured by the forward-scatter visibility sensor with a
230 wavelength of 550 nm. The scattering angle of the sensor ranges from 0 to 45 degree, the sampling
231 volume is 0.75 cubic feet and the response time is 20 seconds. The sensor provides 1-minute average
232 visibility with the day or night indication. Hourly visibility is calculated based on the harmonic
233 average of minutely visibility. Experiments have found that harmonic average visibility can better
234 detect the development of some weather phenomena than arithmetic average visibility (NOAA et
235 al., 1998). The sensor-measured visibility has a strong agreement with the human-observed during
236 haze and homogeneous weather over a large area, even during periods when weather conditions are



237 quite variable (NOAA et al., 1998). The same algorithm is used to calculate the daily, monthly,
238 seasonally and yearly average visibility.

$$239 \quad V = n / \left(\frac{1}{V_1} + \frac{1}{V_2} + \dots + \frac{1}{V_n} \right) \quad \text{Eq. 1}$$

240 where V is the harmonic mean, $n = 24$ for the daily mean, and V_1, V_2, \dots, V_n are the individual
241 hourly values.

242 Visibility in METAR is reported in statute miles (SM). The reportable increments are: M1/4SM,
243 1/4SM, 1/2SM, 3/4SM, 1SM, 1 1/4SM, 1 1/2SM, 1 3/4SM, 2SM, 2 1/2SM, 3SM, 4SM, 5SM, 6SM,
244 7SM, 8SM, 9SM and 10SM. It is noted that visibility between zero and 1/4 statute mile is reported
245 as M1/4SM8. Visibility values of exactly halfway between reportable values are rounded down.
246 Visibility values of 10 miles or greater are reported as 10SM (NOAA et al., 1998).

247 In addition to hourly visibility (VIS), we also selected other automatically observed variables
248 closely related to aerosol properties in this study. Because relative humidity influences the size and
249 hygroscopic growth rate of particle matter, and wind speed and pressure significantly impact the
250 transport and deposition of aerosols, relative humidity (RH), dew point temperature (DT),
251 temperature (TMP), wind speed (WS) and sea-level pressure (SLP) are adopted. Additionally, sky
252 conditions (cloud amount) and hourly precipitation are also selected to remove the influence of
253 extensive cloud cover and precipitation when deriving AOD.

254 We processed the data as follows. The records with missing values were eliminated (Husar et al.,
255 2000). When over 80% overcast or fog, the records of sky conditions were eliminated, though such
256 situations occur less than 1% of the time over land (Remer et al., 2008). The records with 1-hour
257 precipitation greater than 0.1 mm were eliminated. The records with RH greater than or equal to 90%
258 were eliminated. We calculate the temperature dew point difference (dT). When RH is between 30%
259 and 90%, visibility is converted to dry visibility (Yang et al., 2021c).

$$260 \quad \text{VISD} = \text{VIS} / (0.26 + 0.4285 * \log(100 - \text{RH})) \quad \text{Eq. 2}$$

261 where VISD is the dry visibility.

262 Daily average of variables are calculated by at least 3 hourly records with a harmonic mean for
263 visibility (NOAA et al., 1998) and an arithmetic mean for the other variables.

264 **2.3 Boundary layer height**

265 The hourly boundary layer height (BLH) from 1980 to 2021 is available from the Fifth Generation
266 European Medium-Range Weather Forecast Center (ERA5) with a resolution of $0.25^\circ \times 0.25^\circ$
267 (<https://cds.climate.copernicus.eu>), which is the successor of ERA-Interim and has undergone
268 various improvements (Hersbach et al., 2020). The atmospheric boundary layer is the layer closest
269 to the Earth's surface and exhibits complex turbulence activities, and its height undergoes significant
270 diurnal variation. The effects of the boundary layer on aerosols are mainly manifested in vertical
271 distribution, concentration changes, transport, and deposition (Ackerman et al., 1995). The
272 characteristics and variations in the boundary layer play a crucial role in regulating and adjusting
273 the distribution of atmospheric aerosols. The boundary layer height serves as an approximate
274 measure of the scale height for aerosols (Zhang et al., 2020). The BLH of ERA5 is considered to be



275 the more promising dataset compared to the MERRA-2, JRA-55, and NCEP-2 datasets (Guo et al.,
276 2021). The BLH data is temporally and spatially matched with the ASOS stations. Because the
277 inverse of visibility is proportional to the extinction coefficient and positively related to AOD (Wang
278 et al., 2009) and the atmospheric aerosols are largely distributed in the boundary layer (Zhang et al.,
279 2020), three variables (VISI, VISDI, VISDIB) are increased, shown in Eq. 3 :

$$280 \quad VISI = \frac{1}{VIS}, VISDI = \frac{1}{VISD}, VISDIB = VISDI * BLH \quad \text{Eq. 3}$$

281 Thus, the Predictors (Figure 2) is composed of 11 variables: TMP, Td, dT, RH, SLP, WS, VIS, BLH,
282 VISI, VISDI, and VISDIB.

283 2.4 MODIS AOD Products

284 Satellite daily AOD is available from the Moderate Resolution Imaging Spectroradiometer (MODIS)
285 Level 3 Collection 6.1 AOD products of the Aqua (MYD09CMA) satellite from 2002 to 2021 and
286 Terra (MOD09CMA) satellite from 2000 to 2021 with a spatial resolution of $0.05^\circ \times 0.05^\circ$ at a
287 wavelength of 550 nm (<https://ladsweb.modaps.eosdis.nasa.gov>). MOD/MYD09 has a higher
288 spatial resolution than MOD/MYD08 ($1^\circ \times 1^\circ$), which may result in a greater difference in AOD
289 values and reduce the proximity ratio to match the same AOD value. Terra (passing approximately
290 10:30 am local time) and Aqua (passing approximately 1:30 pm local time) were successfully
291 launched in December 1999 and May 2002, respectively. MODIS, carried on the Terra and Aqua
292 satellites is a crucial instrument in the NASA Earth Observing System program, which is designed
293 to observe global biophysical processes (Salomonson et al., 1987). The 2,330 km-wide swath of the
294 orbit scan can cover the entire globe every one to two days. MODIS has 36 channels and more
295 spectral channels than previous satellite sensors (such as AVHRR). The spectral range from 0.41 to
296 $15 \mu\text{m}$ representing three spatial resolutions: 250 m (2 channels), 500 m (5 channels), and 1 km (29
297 channels). The aerosol retrieval uses seven of these channels ($0.47\text{--}2.13 \mu\text{m}$) to retrieve aerosol
298 characteristics and uses additional wavelengths in other parts of the spectrum to identify clouds and
299 river sediments. Therefore, it has the ability to characterize the spatial and temporal characteristics
300 of the global aerosol field. The MODIS aerosol product actually takes use of different algorithms
301 for deriving aerosols over land and ocean. The Dark Target (DT) algorithm is applied to densely
302 vegetated areas because the surface reflectance over dark-target areas was lower in the visible
303 channels and had nearly fixed ratios with the surface reflectance in the shortwave and infrared
304 channels (Levy et al., 2007; Levy et al., 2013). The Deep Blue (DB) algorithm was originally
305 applied to bright land surfaces (such as deserts), and later extended to cover all cloud-free and snow-
306 free land surfaces (Hsu et al., 2006; Hsu et al., 2013). MODIS Collection 6.1 aerosol product was
307 released in 2017, incorporating significant improvements in radiometric calibration and aerosol
308 retrieval algorithms. The expected errors are $\pm (0.05 \pm 15\%)$ for the DT retrievals over land. Higher
309 spatial coverage is observed in August and September, reaching 86-88%. During December and
310 January, due to the presence of permanent ice and snow cover in high-latitude regions of the
311 Northern Hemisphere, the spatial coverage is 78-80%. Thus, challenges remain in retrieving AOD
312 values in high-latitude regions (Wei et al., 2019a). However, visibility observations are available in
313 high-latitude regions, thereby partially addressing the lack in these regions. In this study, the Terra
314 and Aqua MODIS AOD are temporally and spatially matched with the ASOS stations. Aqua MODIS
315 AOD is used as the Target, when training the model, and Terra MODIS AOD is used in the
316 evaluation and validation of the model results, as shown in the flowchart (Figure 2).



317 2.5 Ground-based AOD

318 Ground-based daily AOD data are available from the Aerosol Robotic Network (AERONET)
319 Version 3.0 Level 2.0 product at 573 stations (Figure 1), which can be downloaded from
320 <https://aeronet.gsfc.nasa.gov>. The AERONET program is a federation of ground-based remote
321 sensing aerosol networks established by NASA and PHOTONS, including many subnetworks (such
322 as AeroSpan, AEROCAN, NEON, and CARSONET). The sun photometer (CE-318) measures
323 spectral sun and sky irradiance in the 340-1020 nm spectral range. When the aerosol loading is low,
324 the error is significant. When the AOD at 440 nm wavelength is less than 0.2, the error is 0.01,
325 which is equivalent to the error of the absorption band in the total optical depth (Dubovik et al.,
326 2002a). The total uncertainty in AOD under cloud-free conditions is less than ± 0.01 for wavelength
327 more than 440 nm, and ± 0.02 for wavelength less than 440 nm (Holben et al., 1998). AERONET
328 has three levels of AOD products: Level 1.0 (unscreened), Level 1.5 (cloud screened), and Level
329 2.0 (cloud screened and quality assured). Compared to Version 2, the Version 3 Level 2.0 database
330 has undergone further cloud screening and quality assurance, which is generated based on Level 1.5
331 data with pre- and post-calibration and temperature adjustment and is recommended for formal
332 scientific research (Giles et al., 2019). AERONET provides AOD products at wavelengths of 440,
333 675, 870, and 1020 nm. To match the MODIS AOD, the AOD measured from AERONET needs to
334 be converted to the AOD at 550 nm using the Ångström equations (Fan & Sun, 2023).

$$335 \quad \tau_{\alpha}(\lambda) = \beta \lambda^{-\alpha} \quad \text{Eq. 4}$$

$$336 \quad \alpha = -\frac{\ln(\tau(\lambda_1)/\tau(\lambda_2))}{\ln(\tau(\lambda_1)/\tau(\lambda_2))} \quad \text{Eq. 5}$$

$$337 \quad \beta = \frac{\tau(\lambda_1)}{\lambda_1^{-\alpha}} \quad \text{Eq. 6}$$

338 where $\tau_{\alpha}(\lambda)$ is the AOD at a wavelength of 550 nm, β is the turbidity coefficient, α is the
339 wavelength index, and λ_1 and λ_2 are the wavelengths of the two selected channels in AERONET.

340 2.6 Decision Tree Regression

341 2.6.1 Feature selection

342 Although a multidimensional dataset can provide as much potential information as possible for
343 AOD, irrelevant and redundant variables can also introduce significant noise in the model and
344 reduce the model's accuracy and stability (Kang et al., 2021; Dong et al., 2023). Therefore, the F-
345 test is used to search for the optimal feature subset in the Predictor, aiming to eliminate irrelevant
346 or redundant features and select truly relevant features, which helps to simplify the model's input
347 and improve the model's prediction ability (Dhanya et al., 2020). The F-test is a statistical test that
348 gives an f-score ($= -\log(p)$, p represents the degree to which the null hypothesis is not rejected) by
349 calculating the ratio of variances. In this study, we calculate the ratio of variance between the
350 Predictors and Target, and the features are ranked based on higher values of the f-score. A greater
351 value of f-score means that the distances between Predictors and Target are less and the relationship
352 is closer, thus, the feature is more important. We set $p=0.05$. When the score is less than $-\log(0.05)$,
353 the variable in the Predictors is not considered.



354 2.6.2 Data balance

355 Under good weather conditions (such as clear weather), the observed AOD values are concentrated
356 around the average value. Under bad weather conditions (such as heavy haze, wildfires, sandstorms), the
357 value values will vary significantly compared to the good weather conditions, and the frequency of large
358 AOD value is low. When the AOD time series is observed under both good and bad weather conditions,
359 the minority class is large AOD value. This is a phenomenon of data imbalance. When dealing with
360 imbalanced datasets, because of the tendency of machine learning algorithms to perform better on the
361 majority class and overlook the minority class, the model can be underfit (Chuang & Huang, 2023). Data
362 augmentation techniques are commonly employed to address the issue in imbalance data, which applies
363 a series of transformations or expansions to generate new training data, thereby increasing the diversity
364 and quantity of the training data. The Adaptive Synthetic Sampling (ADASYN) is a data augmentation
365 technique specifically designed to address data imbalance problem (He et al., 2008; Mitra et al., 2023).
366 It is an extension of the Synthetic Minority Over-sampling Technique (SMOTE) algorithm (Fernández
367 et al., 2018). The goal of ADASYN is to generate synthetic sample data for the minority class to increase
368 its representation in the dataset. ADASYN, which adaptively adjusts the generation ratio of synthetic
369 samples based on the density distribution of sample data, improves the dataset balance and enhances the
370 performance of machine learning models in dealing with imbalanced data.

371 2.6.3 Decision Tree Regression Model

372 The decision tree is a machine learning algorithm based on a tree-like structure used to solve
373 classification and regression problems. We adopt the CART algorithm to construct a regression tree by
374 analyzing the mapping relationship between object attributes (Predictors) and object values (Target). The
375 internal nodes have binary tree structures with feature values of "yes" and "no". In addition, each leaf
376 node represents a specific output for a feature space. The advantages of the regression tree include the
377 ability to handle continuous features and the ease of understanding the generated tree structure (Teixeira,
378 2004; Steinberg & Colla, 2009). Before training the tree model, the variables (Input) are normalized to
379 improve model performance, and after prediction, the results are obtained by denormalization. The 10-
380 fold cross-validation method is employed to improve the generalization ability of the model (Browne,
381 2000).

382 The core problems of the regression tree need to solve are to find the optimal split variable and optimal
383 split point. The optimal split point of Predictors is determined by the minimum MSE, which in turn
384 determines the optimal tree structure. We set $Y = [y_1, y_2, \dots, y_N]$ as the Target. We set $X =$
385 $[x_1, x_2, \dots, x_N]$ as the Predictors, $x_i = (x_i^1, x_i^2, \dots, x_i^n)$, $i = 1, 2, 3, \dots, N$, where n is the feature number, and
386 N is the length of sample. We set a training dataset as $D = [(x_1, y_1), (x_2, y_2), \dots, (x_N, y_N)]$.

387 A regression tree corresponds to a split in the feature space and the output values on the split domains.
388 Assuming that the input space has been divided into M domains $[R_1, R_2, \dots, R_M]$ and there is a fixed
389 output value on each R_m domain, the regression tree model can be represented as follows:

$$390 \quad f(x) = \sum_{m=1}^M c_m I(x \in R_m), m = 1, 2, \dots, M \quad \text{Eq. 7}$$

391 where I is the indicator function (Eq. 8).

$$392 \quad I = \begin{cases} 1, & x \in R_m \\ 0, & x \notin R_m \end{cases} \quad \text{Eq. 8}$$



393 When the partition of the input space is determined, the square error can be used to represent the
 394 prediction error of the regression tree for the training data, and the minimizing square error is used to
 395 solve the optimal output value on each domain. The optimal value (\widehat{c}_m) on a domain is the mean of the
 396 outputs corresponding to all input, namely:

$$397 \quad \widehat{c}_m = \text{ave}(y_i | x_i \in R_m) \quad \text{Eq. 9}$$

398 A heuristic method is used to split the feature space in CART. After each split, all values of all features
 399 in the current set are examined individually, and the optimal one is selected as the split point based on
 400 the principle of minimum sum of the square errors. The specific step is described as follows: for the
 401 training dataset D , we recursively divide each region into two sub domains and calculate the output
 402 values of each sub domain; then, construct a binary decision tree. For example, split variable is x^j and
 403 split point is s . Then, in the domain $R_1(j, s) = [x | x^j \leq s]$ and domain $R_2(j, s) = [x | x^j > s]$, we can
 404 solve the loss function $L(j, s)$ to find the optimal j and s .

$$405 \quad L(j, s) = \sum_{x_i \in R_1(j, s)} (y_i - c_1)^2 + \sum_{x_i \in R_2(j, s)} (y_i - c_2)^2 \quad \text{Eq. 10}$$

406 When $L(j, s)$ is the smallest, x^j is the optimal split variable and s is the optimal split point for the
 407 x^j .

$$408 \quad \min_{j, s} \left[\min_{c_1} \sum_{x_i \in R_1(j, s)} (y_i - c_1)^2 + \min_{c_2} \sum_{x_i \in R_2(j, s)} (y_i - c_2)^2 \right] \quad \text{Eq. 11}$$

409 We use the optimal split variable x^j and the optimal split point s to split the feature space and calculate
 410 the corresponding output value.

$$411 \quad \widehat{c}_1 = \text{ave}(y_i | x_i \in R_1(j, s)), \quad \widehat{c}_2 = \text{ave}(y_i | x_i \in R_2(j, s)) \quad \text{Eq. 12}$$

412 We traverse all input variables to find the optimal split variable x^j , forming a pair (j, s) . Divide the
 413 input space into two regions accordingly. Next, repeat the above process for each region until the stop
 414 condition is met. The regression tree is generated.

415 Therefore, the regression tree model $f(x)$ can be represented as follows:

$$416 \quad f(x) = \sum_{m=1}^M \widehat{c}_m I(x \in R_m), \quad m = 1, 2, \dots, M \quad \text{Eq. 13}$$

417 2.7 Gridding method

418 Kriging is a regression algorithm to model and predict (interpolate) random processes/fields based on the
 419 covariance function, which is widely used in geo-statistics (Pebesma, 2004). Ordinary Kriging is the
 420 earliest and most extensively studied form of Kriging. It is a linear estimation system applicable to any
 421 intrinsic stationary random field that satisfies the assumption of isotropy. The two key parameters of
 422 Ordinary Kriging are the semi-variogram function and the weight factors (Goovaerts, 2000). It has been
 423 widely applied in fields, such as climatology, environmental science, and agriculture (Lapen & Hayhoe,
 424 2003; Chen et al., 2010), due to high accuracy, stability, and insensitivity to data shape and distribution.
 425 This study utilizes area-weighted ordinary kriging algorithm to estimate the unknown values of AOD at
 426 specific locations to generate gridded AOD. The longitude range is between -180° E and 180° E, the
 427 latitude range is between -60° N and 85° N, and the spatial resolution is $0.5^\circ \times 0.5^\circ$.

428 2.8 Evaluation metrics

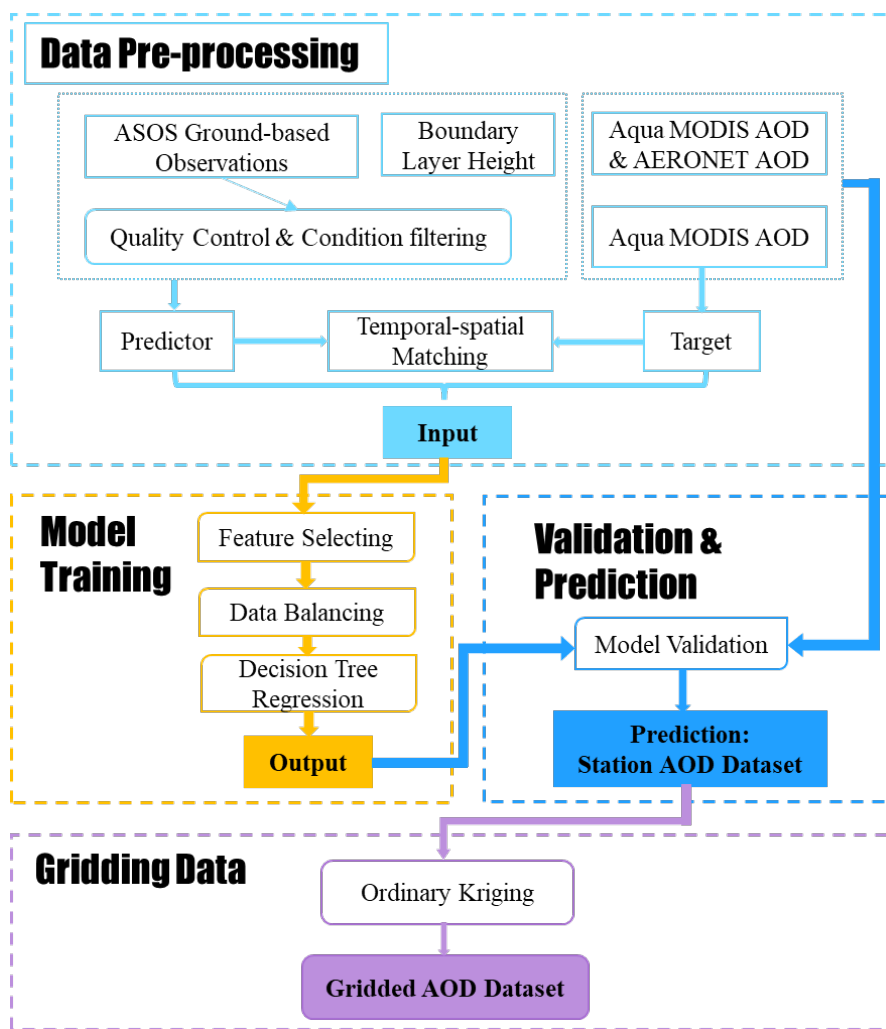


429 Evaluation metrics, including Root Mean Squared Error (RMSE), Mean Absolute Error (MAE) and
 430 Pearson Correlation Coefficient (R), are used to measure the performance and accuracy of the model and
 431 gridded results.

432
$$RMSE = \sqrt{\frac{1}{n} \sum_{i=1}^n (y_i - \hat{y}_i)^2} \quad \text{Eq. 14}$$

433
$$MAE = \frac{1}{n} \sum_{i=1}^n |y_i - \hat{y}_i| \quad \text{Eq. 15}$$

434
$$R = \frac{\sum_{i=1}^n (y_i - \bar{y})(\hat{y}_i - \bar{\hat{y}})}{\sqrt{(\sum_{i=1}^n (y_i - \bar{y})^2) (\sum_{i=1}^n (\hat{y}_i - \bar{\hat{y}})^2)}} \quad \text{Eq. 16}$$



435

436 **Figure 2** Flowchart for deriving aerosol optical depth (AOD).

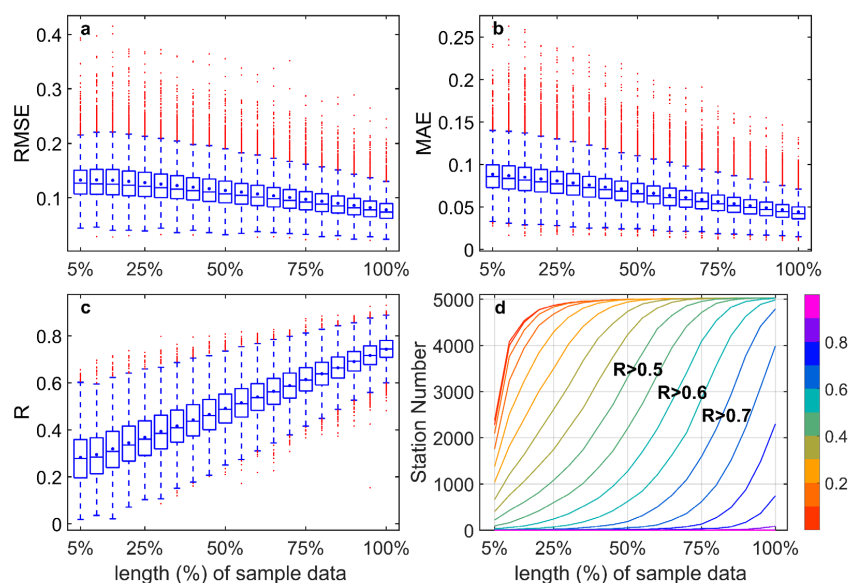


437 2.9 Workflow

438 Figure 2 is the summarized flowchart and provides an overview of the structure of this study, which
439 involves four main parts: (1) data preprocessing, (2) model training, (3) validation and prediction,
440 and (4) data gridding.

441 3 Results and discussion

442 3.1 Examination of the model performance



443

444 **Figure 3** Boxplots of root mean squared error (RMSE) (a), mean absolute error (MAE) (b), and
445 correlation coefficient (R) (c) between predicted values and target using different lengths of sample
446 data (5% interval) as the training dataset, and the correlation coefficient curve (d) of the station
447 number in the different lengths of sample data.

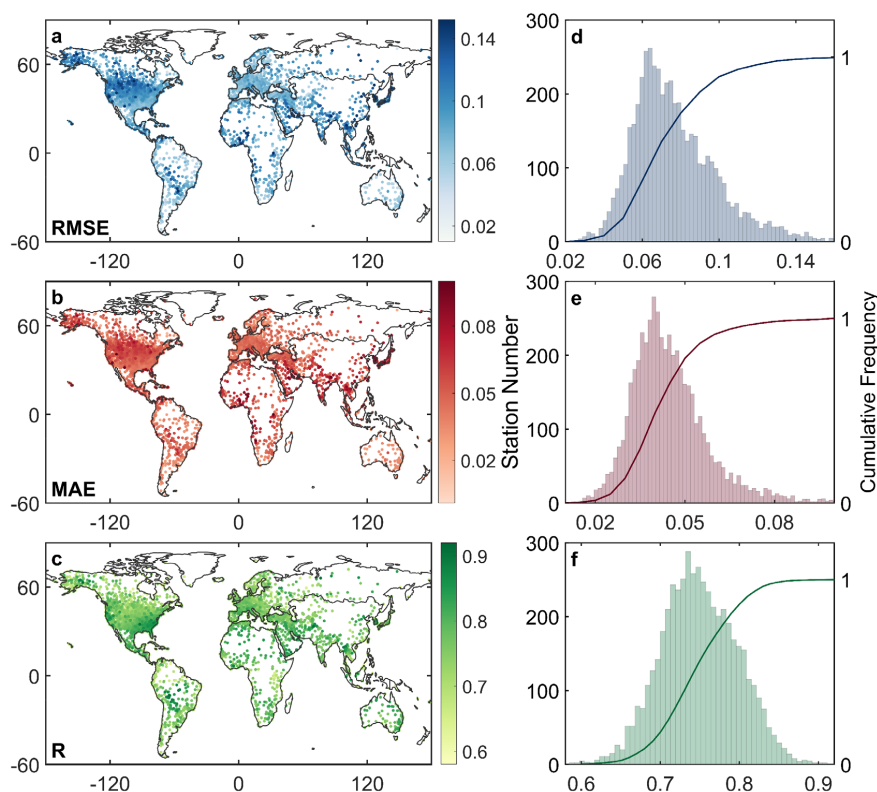
448 We build the models using different lengths of sample data (5% to 100%, with a 5% interval) by random
449 allocation without overlap and evaluate the predictive performance of each model. Figure 3 depicts
450 RMSE(a), MAE(b), and R (c) between the predicted values and target based on the training data of 5%
451 to 100% sample data at a station. As the volume of the training data increases, the RMSE and MAE
452 decrease, and the correlation coefficient increases. Compared to 5% of the sample data, the result of 100%
453 sample data shows a decrease in RMSE by 41.1%, a decrease in MAE by 50.1%, and an increase in R
454 by 162.3%. The relationship between the length of sample data and the model's performance is positive
455 for each station. Figure 3 (d) shows that R of approximately 70% stations is greater than 0.5 at 50% of
456 the sample data, while at 75%, the R of approximately 80% of stations is greater than 0.6. When 100%
457 of the sample data is used as sample data, the R of approximately 80% of stations is greater than 0.75,
458 and the R of about 97% is greater than 0.7. This finding indicates that the predictive capability and



459 robustness of the model increase as the amount of training data increases. It may be attributed to the
460 model's ability to capture more complex patterns and relationships among the input by multi-year data.

461 3.2 Evaluation of model errors

462 The more sample data input, the better the model performs. Therefore, 100% of the sample data were
463 used as training data. Figure 4 shows the spatial distribution (a-c) and frequency and cumulative
464 frequency (d-e) of RMSE, MAE, and R of all stations. The mean values of RMSE, MAE, and R are 0.078,
465 0.044, and 0.75, respectively. The RMSE of 93% stations is less than 0.11, the MAE of 91% is less than
466 0.06, and the R of 88% is greater than 0.7. The R values in Africa, Asia, Europe, North America, Oceania,
467 and South America are 0.763, 0.758, 0.736, 0.750, 0.759, and 0.738, respectively. Although the RMSE
468 and MAE of a few stations are high in America and Asia, the R is still high (>0.6). Therefore, the results
469 of the model's errors demonstrate that the model performs well on almost all stations.



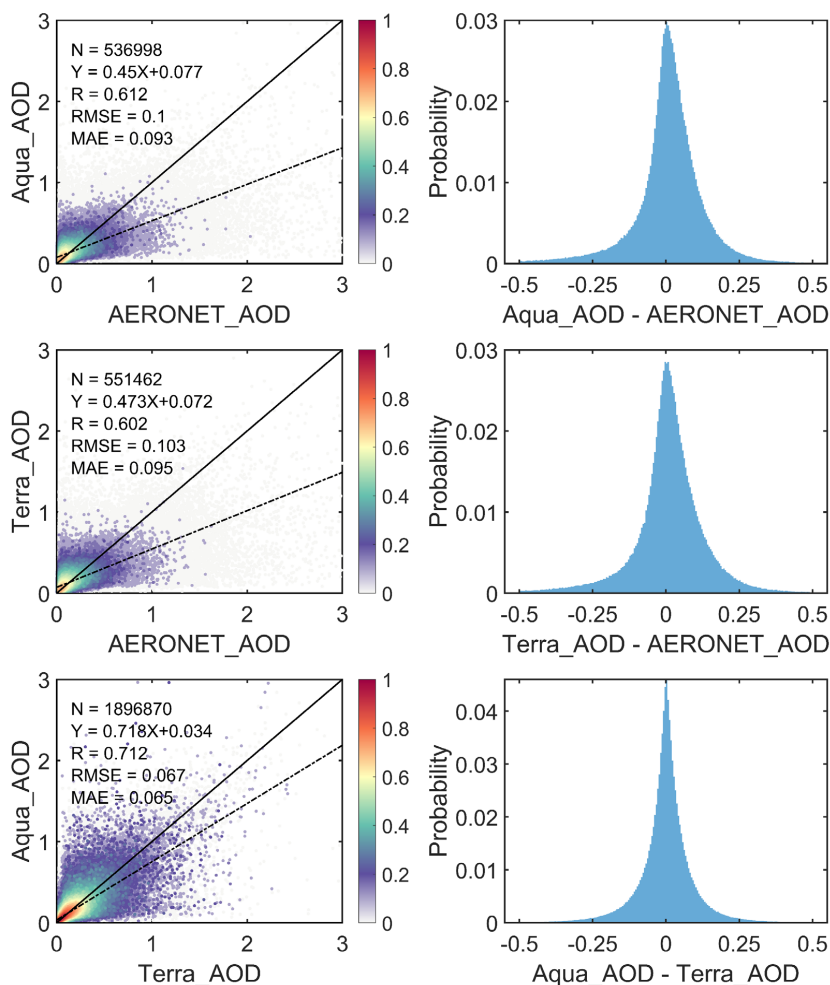
470
471 **Figure 4** Spatial distribution (a-c) of root mean squared error (RMSE), mean absolute error (MAE),
472 and correlation coefficient(R) between the model's result and target with 100% sample data. Station
473 number (bar) and cumulative frequency (curve) (d-e) of RMSE, MAE, and R.

474 3.3 Validation of derived AOD against MODIS and AERONET AOD

475 First, the relationship among daily MODIS and AERONET AOD is evaluated. Figure 5 presents the
476 scatter density plots (the left column) and bias probability distribution (the right column) among daily



477 Aqua, Terra and AERONET AOD. The R, RMSE, and MAE of 536,998 data couples between Aqua AOD
478 and AERONET AOD are 0.612, 0.1, and 0.093, respectively. Then, 86.8% of the data have a bias within
479 ± 0.093 . The R, RMSE, and MAE of 551,462 data couples between Terra AOD and AERONET AOD are
480 0.602, 0.103, and 0.095, respectively. Then 86% of the data have a bias within ± 0.095 . The R, RMSE,
481 and MAE of 1,896,870 data couples between Aqua AOD and Terra AOD are 0.712, 0.067, and 0.065,
482 respectively, and the bias is within ± 0.065 for 92% of the data. On the global scale, the AOD retrieved
483 by satellites may be overestimated at low AOD levels and underestimated at high AOD levels compared
484 to AERONET AOD. Approximately 86% of the bias values are less than the MAEs. Terra and Aqua have
485 good consistency, although one is for morning transit and the other is for afternoon transit. Finally, 92%
486 of the data bias are less than the MAEs. Thus, there is good consistency among them on the daily scale.



487

488 **Figure 5** Scatter density plots and bias probability between Aqua AOD, Terra AOD and AERONET
489 AOD at a daily scale. The solid black line represents the 1:1 line and the dashed black line is the

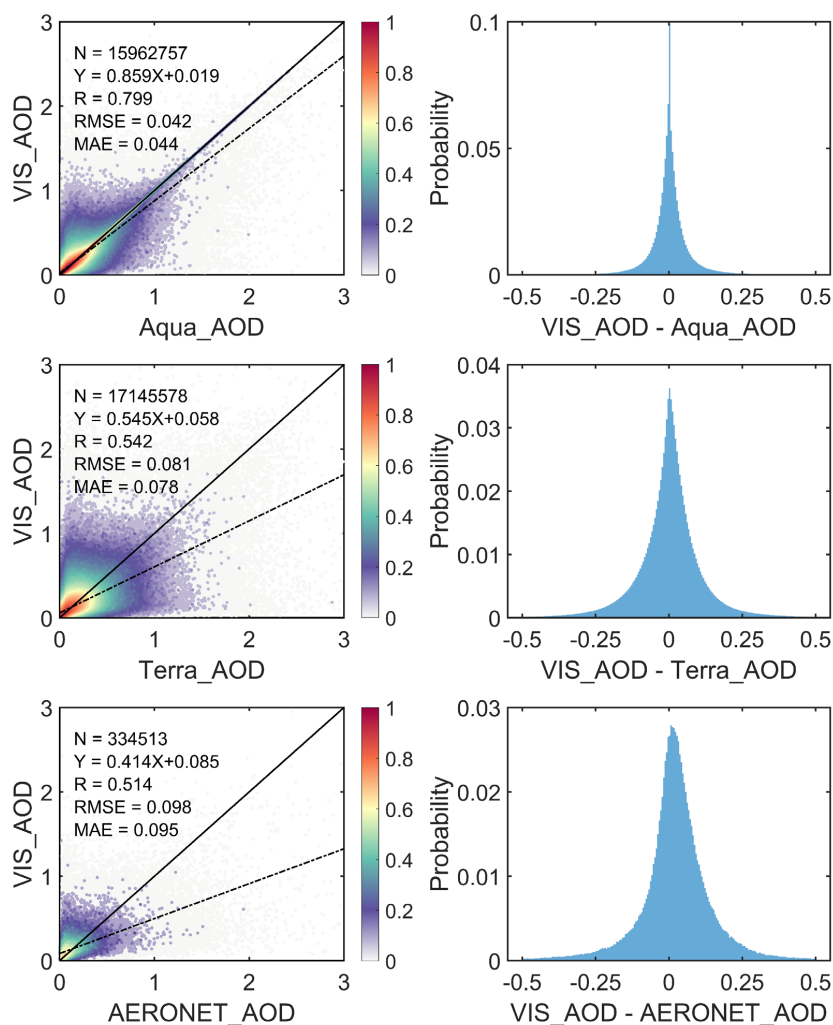


490 linear regression line.

491 To validate the model's predictive ability, the visibility-derived AOD (for short, VIS_AOD) is compared
492 with other observed data for daily, monthly, and yearly scales of Aqua, Terra and AERONET AOD.
493 Figure 6 shows the scatter density plots and probability distribution of the bias between daily VIS_AOD
494 and Aqua AOD, Terra AOD, and AERONET AOD. The R of 15,962,757 pairs data between VIS_AOD
495 and Aqua AOD is 0.799, higher than the R between AERONET AOD and Aqua AOD, as well as Terra
496 AOD and Aqua AOD. The RMSE is 0.042 and the MAE is 0.044. Then, 69.7% of the data pairs have a
497 bias within ± 0.044 , and 69.7% have a bias within ± 0.093 . The R of 17,145,578 pairs of data between
498 VIS_AOD and Terra AOD is 0.542, the RMSE is 0.081 and the MAE is 0.078. Then, 66.8% of the data
499 pairs have a bias within ± 0.078 , and 73.3% have a bias within ± 0.095 . The R of 334,513 data pairs
500 between VIS_AOD and AERONET AOD is 0.514. The RMSE is 0.098 and the MAE is 0.095. Finally,
501 78.3% of the data pairs have a bias within ± 0.095 .

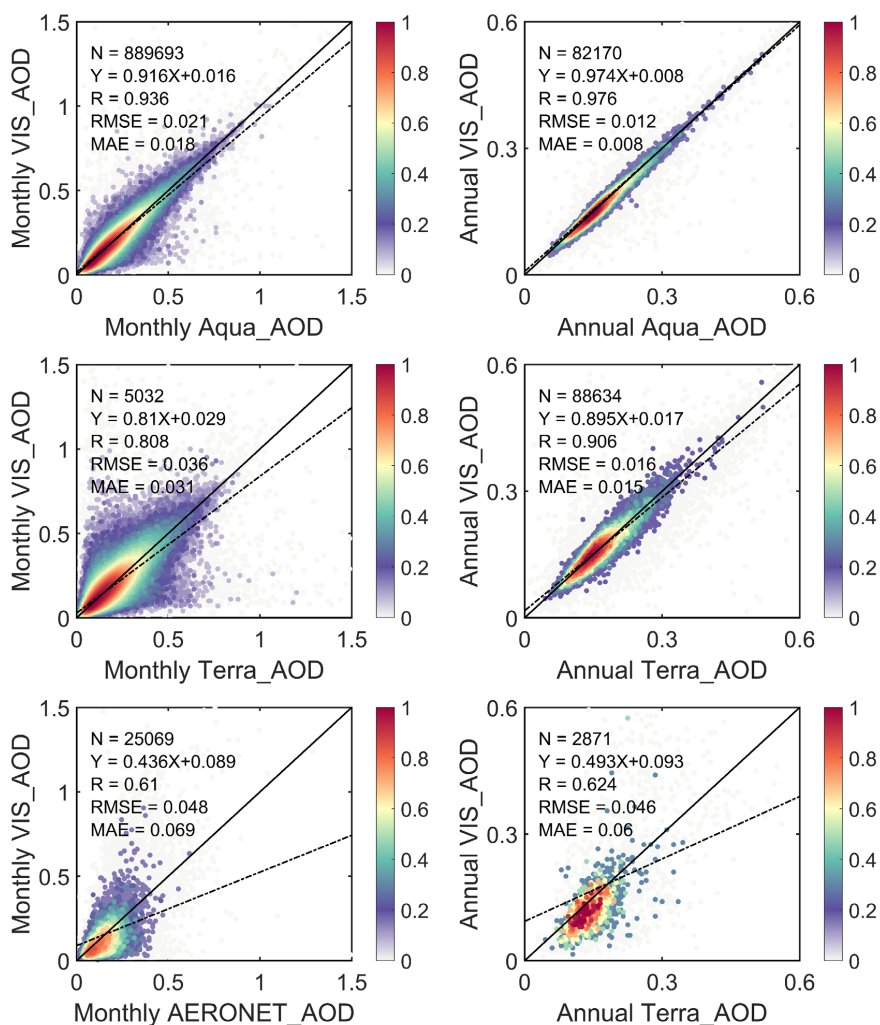
502 At the monthly and annual scales, RMSE and MAE show a significant decrease between VIS_AOD and
503 Aqua, Terra, and AERONET AOD, and R shows a significant increase in Figure 7. The monthly RMSEs
504 are 0.021, 0.036, and 0.048, the monthly MAEs are 0.018, 0.031, and 0.069, and the R values are 0.936,
505 0.808, and 0.61, respectively. The RMSE values at the annual scale are 0.012, 0.016, and 0.025, the MAE
506 values are 0.008, 0.015, and 0.006, and the R values are 0.976, 0.0906, and 0.624, respectively. The
507 monthly and annual R is slightly higher than those in previous studies (Wang et al., 2009; Wu et al., 2014;
508 Zhang et al., 2017). In addition to the differences between models, it may also be related to the calculation
509 method of daily average visibility and the consideration of boundary layer height.

510 Overall, the results highlighted above demonstrate a clear improvement in performance on the monthly
511 and annual scales compared to the daily scale. However, the AERONET AOD results are slightly inferior
512 to those of Aqua and Terra AOD, which could be caused by the representativeness of the AERONET
513 station spatial coverage and measurement error (Holben et al., 1998). Nevertheless, the results indicate
514 the high reliability and strong predicted capability of the model, and the visibility-derived AOD can be
515 used for aerosol climatology.



516

517 **Figure 6** Scatter density plots and bias probability between predicted AOD (VIS_AOD) and Aqua
518 MODIS AOD, Terra MODIS AOD and AERONET ground-based observations of AOD at the daily
519 scale. The solid black line represents the 1:1 line and the dashed black line is the linear regression
520 line.



521

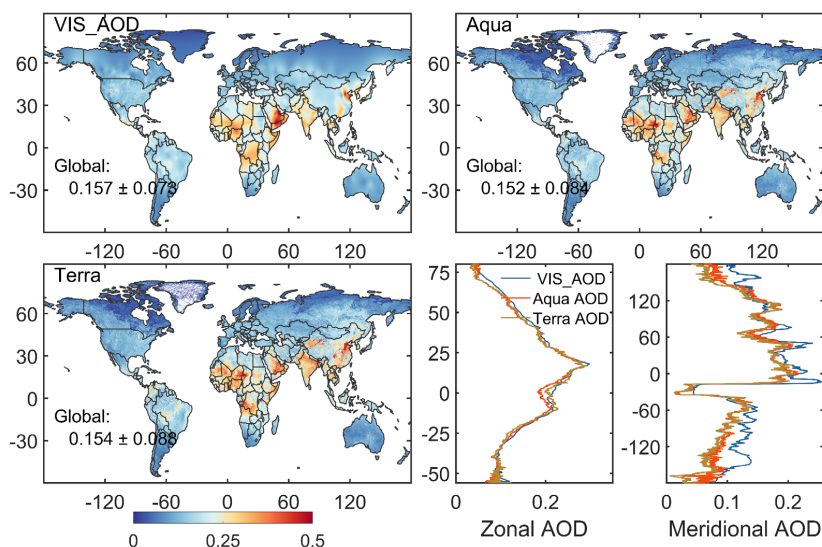
522 **Figure 7** Scatter density plots and bias probability between VIS_AOD and Aqua MODIS AOD,
 523 Terra MODIS AOD and AERONET ground-based observations of AOD at the monthly and annual
 524 scales. The solid black line represents the 1:1 line and the dashed black line is the linear regression
 525 line.

526 **3.4 Evaluation of gridded visibility-derived AOD**

527 Figure 8 shows the gridded AOD based on ordinary kriging interpolation with the area-weighted
 528 method and compares the multi-year spatial, zonal, and meridional distributions of AOD with Aqua
 529 and Terra AOD from 2003 to 2021. The VIS_AOD is 0.157 ± 0.073 over land, which is almost equal
 530 to the Aqua (0.152 ± 0.084) and Terra (0.154 ± 0.088) AOD values with relative biases of 3.3%, and
 531 1.9%, respectively. In order to compare the spatial correlation, Aqua and Terra MODIS AOD are
 532 averaged to the 0.5-degree resolution. In the heatmap (Figure 9), the R of VIS_AOD and Aqua AOD

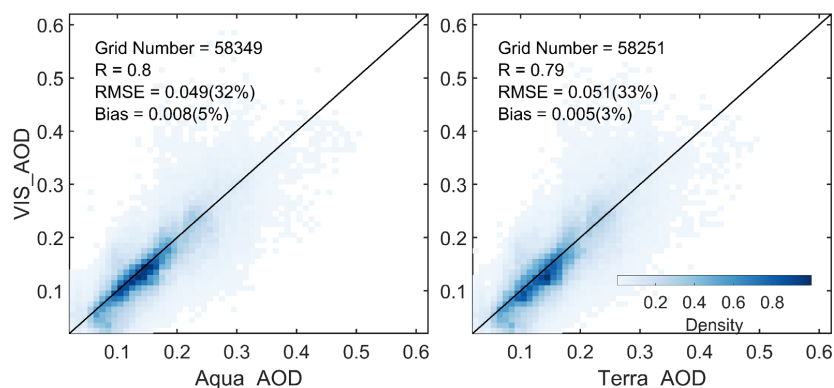


533 is 0.8, the RMSE is 0.049 with a bias of 32% compared to the mean, and the MAE is 0.008, with a
534 bias of 5% compared to the mean. Compared to Terra AOD, the R is 0.79, and the RMSE is 0.051,
535 with a bias of 33% compared to the mean, and the MAE is 0.005, with a bias of 3% compared to
536 the mean. Aqua and Terra AOD are highly similar, with an R of 0.98. By comparing the zonal and
537 meridional distributions of AOD, VIS_AOD is consistent with Aqua and Terra AOD, with the R of
538 0.997 and 0.99 for the zonal distribution and 0.986 and 0.9 for the meridional distribution,
539 respectively. In the low aerosol loading region, VIS_AOD exhibits a little overestimation. Whether
540 in meridional or zonal distribution, the peak and valley regions are basically consistent (Tian et al.,
541 2023). Due to the limitations of satellite inversion algorithms, a bias appears on the bright surface,
542 especially in northern North America with extensive snow cover (Levy et al., 2013). All above
543 results suggest that the gridded AOD is highly consistent with satellite observations in spatial
544 distribution.



545

546 **Figure 8** The spatial, zonal and meridional distributions of the multi-year mean VIS_AOD, Aqua
547 AOD, and Terra AOD from 2003 to 2021.



548

549 **Figure 9** Heatmap of multi-year mean gridded VIS_AOD and Aqua AOD and Terra AOD during
550 2003-2021. Terra and Aqua AOD are averaged onto a grid of 0.5°.

551 3.5 Global spatiotemporal variation of AOD in 1980-2021

552 The evaluation of visibility-derived AOD has demonstrated that the numerical and spatial
553 distributions of VIS_AOD are in good agreement with the observations. Therefore, we employed
554 VIS_AOD to analyze the spatiotemporal and seasonal distributions, and trends over land from 1980
555 to 2021. The analytical findings are shown as follows. The AOD mentioned below is the AOD
556 derived from visibility.

557 We first analyzed the spatial distribution of multi-year average AOD over land from 1980 to 2021
558 and separately for the Southern Hemispheres (SH, -60-0°N) and Northern Hemisphere (NH, 0-85°N)
559 in Figure 10 (a). The mean AOD of land, NH and SH is 0.161 ± 0.074 , 0.158 ± 0.076 , and $0.173 \pm$
560 0.059 , respectively. The AOD values of Africa, Asia, Europe, North America, Oceania, and South
561 America are 0.241, 0.222, 0.11, 0.111, 0.129 and 0.117, respectively. High AOD values occur in the
562 NH, and align with the distribution of population density. Approximately 7/8 of the global
563 population resides in the NH, with 50% concentrated at 20°N-40°N (Kummu et al., 2016), indicating
564 a significant impact of human activities on aerosols. The highest AOD values are observed near
565 17°N, including the Sahara Desert, Arabian Peninsula, and southeastern India, suggesting that in
566 addition to anthropogenic sources, deserts also play a crucial role in aerosol emissions. Lower AOD
567 values are found in the 25°S region of the SH, encompassing Australia, southern Africa, and
568 southern South America, indicating lower aerosol burdens in these areas. Additionally, North
569 America also exhibits low aerosol loading. Chin et al. (2014) analyzed the AOD over land from
570 1980 to 2009 with the Goddard Chemistry Aerosol Radiation and Transport model, which is similar
571 to the visibility-derived AOD. The spatial distribution is consistent with the satellite results (Remer
572 et al., 2008; Hsu et al., 2012; Hsu et al., 2017; Tian et al., 2023). The AOD and extinction coefficient
573 retrieved from visibility show a similar distribution at global scale, with a correlation coefficient of
574 nearly 0.6 (Mahowald et al., 2007). Similar global (Husar et al., 2000; Wang et al., 2009) and
575 regional (Koelemeijer et al., 2006; Wu et al., 2014; Boers et al., 2015; Zhang et al., 2017; Zhang et
576 et al., 2020) spatial distributions have been reported.

577 AOD loadings exhibit significant seasonal variations worldwide, particularly over land. In this study,
578 a year is divided into four parts: December-January-February (DJF), March-April-May (MAM),



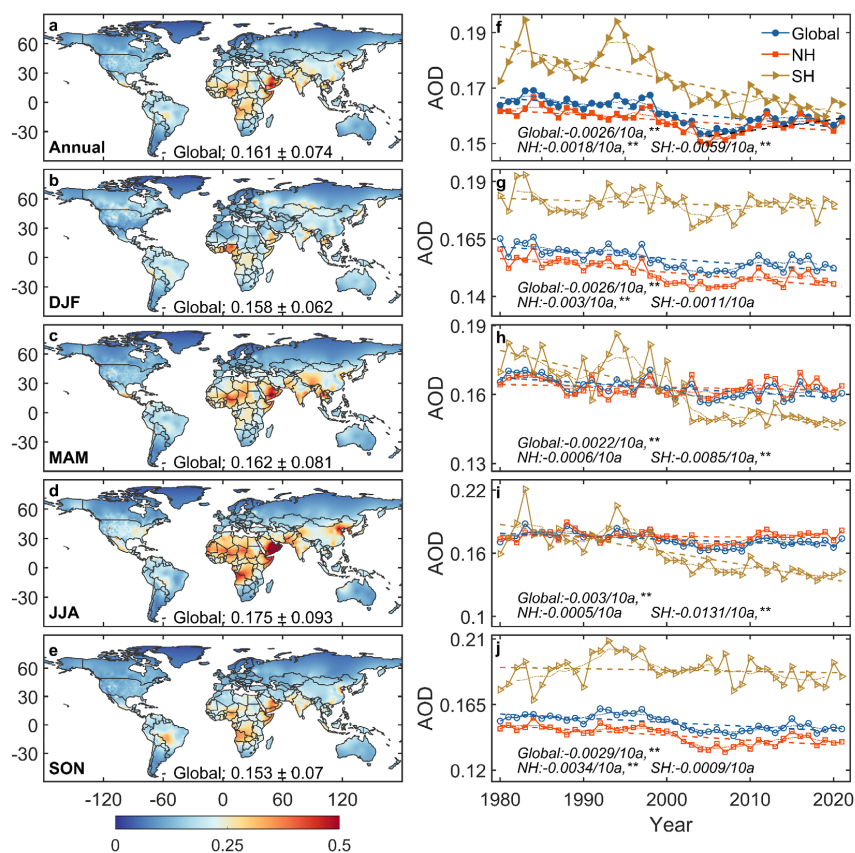
579 June-July-August (JJA), and September-October-November (SON), corresponding to winter
580 (summer), spring (autumn), summer (winter), and autumn (spring) in NH (SH), respectively. Figure
581 10 (b-e) also depicts the spatial distribution of seasonal average AOD over land from 1980 to 2021.
582 The global AOD in DJF, MAM, JJA, and SON is 0.158 ± 0.062 , 0.162 ± 0.081 , 0.175 ± 0.093 , and
583 0.153 ± 0.07 , respectively. The standard deviations of AOD in JJA and MAM are greater than those
584 in DJF and SON. AOD exhibits seasonal changes, with the highest in JJA, followed by MAM, DJF,
585 and SON. From 1980 to 2021, the seasonal AOD in NH is 0.152 ± 0.064 (DJF), 0.161 ± 0.088 (MAM),
586 0.176 ± 0.09 (JJA), and 0.144 ± 0.06 (SON), and in SH is 0.184 ± 0.041 (DJF), 0.166 ± 0.044 (MAM),
587 0.169 ± 0.072 (JJA), and 0.19 ± 0.06 (SON). In NH, the AOD ranking from high to low in season is
588 summer > spring > winter > autumn. In SH, the AOD ranking from high to low in season is spring >
589 summer > winter > autumn. The highest AOD is observed during JJA in NH, while in SH, the peak
590 occurs during SON. The occurrence of high AOD values is highly associated with the intensification
591 of industrial activities in Asia (JJA) (Remer et al., 2008) and Europe such as Russia (JJA), South
592 America (SON), Southern Africa (SON), and biomass burning in Indonesia (SON) (Ivanova et al.,
593 2010; Krylov et al., 2014), and the increased dust emissions in Middle East region related to the
594 transport of dust from the Sahara region (Remer et al., 2008; Prakash et al., 2014). On the other
595 hand, the lowest global AOD values are observed during autumn, which may be attributed to the
596 influence of monsoon systems (Li et al., 2016; Zhao et al., 2019).

597 In addition to the spatial characteristics of AOD, the temporal variations in AOD have also been of
598 great interest due to the significant relationship between aerosols and climate change. Figure 10 (f)
599 shows the temporal trends of annual average AOD (** represents passing the significance test,
600 $p<0.01$) over the global land, the SH and the NH during 1980-2021. The global land, NH, and SH
601 trends demonstrate decreasing trends of AOD with values of $-0.0026/10a$, $-0.0018/10a$, and $-$
602 $0.0059/10a$, respectively, with all passing the significance test with a confidence level of 95%.
603 Notably, the declining trend is much greater in the SH than in the NH. The MODIS satellite results
604 (including oceans) indicate trends of $0.004/10a$, $0.009/10a$, and $-0.002/10a$ for the global, SH, and
605 NH, respectively, during the period of 2003-2020. This findings suggest a growth trend in the global
606 and NH and a declining trend in SH (Tian et al., 2023). The trend of SeaWiFS AOD was $0.0058/10a$
607 over land during 1998-2010 (Hsu et al., 2012). Our study has the same downward signal as that in
608 previous studies. Two AOD peaks in 1983 and 1994 and two AOD valleys in 1980 and 1990 are
609 observed before 2000. The two AOD peaks may be attributed to large volcanic eruptions, which has
610 been confirmed by previous studies. The volcanic eruptions and their associated fires of the El
611 Chichón volcano in Mexico in 1982 (Hirono & Shibata, 1983) and Mount Pinatubo in the
612 Philippines in 1991 (Tupper et al., 2005) resulted in elevating global AOD levels in the following
613 years. The AOD recovery to the previous low levels after volcanic eruptions takes approximately
614 10 years (Chazette et al., 1995; Sun et al., 2019). This further indicates the efficiency of our data
615 capturing the volcanic eruption emission features. also indicates that our data effectively captures
616 this feature.

617 The distinct seasonal trends of AOD during 1980-2021 at the global and hemispheric scales are
618 shown in Figure 10 (g-j). The global AOD shows a decreasing trend in all seasons ($-0.002\sim$
619 $0.003/10a$). The large declining trends are observed in JJA and SON, with decreasing trend values
620 of $-0.003/10a$ and $-0.0029/10a$, respectively. DJF and MAM follow with decreasing trend values of
621 $-0.0026/10a$ and $-0.0022/10a$, respectively, all passing the significance test ($p<0.01$). For the NH,



622 the AOD trends in different seasons are $-0.003/10a$ (DJF), $-0.0006/10a$ (MAM), $-0.0005/10a$ (JJA),
 623 and $-0.0034/10a$ (SON). DJF and SON pass the significance test ($p < 0.01$), while MAM and JJA do
 624 not. In the SH, the trends are as follows: $-0.0011/10a$ (DJF), $-0.0085/10a$ (MAM), $-0.0131/10a$ (JJA),
 625 and $-0.0009/10a$ (SON). Interestingly, in contrast to the NH, MAM and JJA pass the significance
 626 test, while DJF and SON do not. The largest declining season in the NH is winter, while in the SH,
 627 it is summer. The decreasing trend in the SH is more than four times greater than that in the NH,
 628 particularly before the year 2000. While both the global and SH AOD exhibit a decreasing trend
 629 since 2005, the NH has shown a significant increase in winter AOD, leading to an overall increasing
 630 trend. Moreover, the NH shows an increasing trend of $0.004/10a$ from 2005 to 2021. Annual SO_2
 631 emissions increased from 9.4 to 15.3 TgS from 2000 to 2005, which ultimately ended up as sulfate
 632 aerosols, leading to a significant increase in sulfate aerosols (Hofmann et al., 2009). More relevantly,
 633 the frequent volcanic eruptions in tropical regions from 2002 to 2006, combined with seasonal
 634 circulation patterns during winter, led to the transport of aerosol particles to higher latitudes
 635 (Hofmann et al., 2009; Vernier et al., 2011; Sawamura et al., 2012; Andersson et al., 2015).



636

637 **Figure 10** The multi-year averages of VIS_AOD from 1980 to 2021. Global (circle), northern
 638 hemisphere (NH, 0-85°N) (triangle) and southern hemisphere (SH, 0-60°S) (square) annual and
 639 seasonal AOD. The symbol, **, represents that the test passed at a significance level of 0.01. DJF



640 represents December and next January and February. MAM represents March, April, and May. JJA
641 represents June, July, and August. SON represents September, October, and November.

642 **3.6 Regional spatiotemporal variation in AOD during 1980-2021**

643 The distribution of AOD over global land exhibits significant spatial heterogeneity. Large variations
644 in aerosol concentrations exist among different regions, leading to a non-uniform spatial distribution
645 of AOD globally. Accurately assessing the long-term trends of aerosol loading is a key for
646 quantifying aerosol climate change, and it is crucial for evaluating the effectiveness of measures
647 implemented to improve regional air quality and reduce anthropogenic aerosol emissions.

648 To analyze the spatiotemporal characteristics and trends of AOD in different regions, we selected
649 12 representative regions that are influenced by various aerosol sources (Wang et al., 2009; Hsu et
650 al., 2012; Chin et al., 2014), such as desert, industry, anthropogenic emissions, and biomass burning
651 emissions, which nearly cover the most land and are densely populated regions (Kummu et al., 2016).
652 These representative regions are Eastern Europe, Western Europe, Western North America, Eastern
653 North America, Central South America, Western Africa, Southern Africa, Australia, Southeast Asia,
654 Northeast Asia, Eastern China, and the Middle East, as shown in Figure 1.

655 We use multi-year average and seasonal average AOD to evaluate aerosol loadings (Figure 11), the
656 annual average of monthly anomalies to analyze interannual trends (Figure 12), and the seasonal
657 average to analyze seasonal trends (Figure 13) in 12 regions from 1980 to 2021.

658 Figure 11 shows the regions with high aerosol loadings from 1980 to 2021 (multi-year average
659 AOD > 0.2) are in West Africa, Northeast Asia, Eastern China, and the Middle East. The AOD
660 values in Eastern North America, Central South America, South Africa, and Southeast Asia range
661 from 0.15 to 0.2 with middle aerosol loadings. The AOD values in Eastern Europe, Western Europe,
662 Western North America, and Australia are less than 0.15 with low aerosol loadings.

663 Europe is an industrial region with a low aerosol loading region, and the multi-year average AOD
664 in Eastern Europe (0.144 ± 0.007) is higher than that in Western Europe (0.139 ± 0.003) during 1980-
665 2021. Eastern Europe shows a greater downward trend in AOD ($-0.0041/10a$) compared to Western
666 Europe ($-0.0021/10a$). The highest AOD is observed in JJA, the dry period when solar irradiation
667 and boundary layer height increase, with Eastern Europe at 0.161 and Western Europe at 0.162,
668 which could be due to increases in secondary aerosols, biomass burning, and dust transport from
669 the Sahara (Mehta et al., 2016). However, there are seasonal variations. In Eastern Europe, the
670 seasonal AOD ranking from high to low is JJA (0.161) > DJF (0.147) > MAM (0.138) > SON
671 (0.131), while in Western Europe, it is JJA (0.162) > MAM (0.140) > SON (0.136) > DJF (0.117).
672 The differences among seasons are larger in Western Europe. AOD in Eastern Europe shows
673 declining trends in all seasons, while it does not pass the significance test in MAM. Among four
674 seasons, SON has the largest decline trend of AOD ($-0.0058/10a$). In Western Europe, DJF, JJA, and
675 SON exhibit declining trends of AOD that pass the significance test, while the MAM shows a
676 significant increase trend of AOD ($0.0022/10a$), which may be due to eruptions of the
677 Eyjafjallajökull volcano in Iceland in spring 2010 (Karbowska & Zembrzuski, 2016). Both Western
678 and Eastern Europe experienced increasing trends in AOD during the period of 1995-2005, with
679 Western Europe showing a greater increase. However, after 2000, the decline rate accelerated in
680 both regions. The downward trend in Europe is attributed to the reduction of biomass burning,



681 anthropogenic aerosols, and aerosol precursors (such as sulfur dioxide)(Wang et al., 2009; Chin et
682 al., 2014; Mortier et al., 2020).

683 North America is also an industrial region with a low aerosol loading. The average AOD values for
684 Eastern and Western North America during 1980-2021 are 0.153 ± 0.004 and 0.131 ± 0.005 ,
685 respectively, with the Eastern region being higher than the Western region by 0.022. From 1980 to
686 2021, both Eastern ($-0.0021/10a$) and Western North America ($-0.0009/10a$) show a downward trend;
687 however, the decline in the Western region is not statistically significant. The average AOD values
688 in DJF, MAM, JJA, and SON in Western North America are 0.1367, 0.1286, 0.1457, and 0.114,
689 respectively, compared to 0.137, 0.145, 0.1913, and 0.138 in Eastern North America. The lowest
690 AOD values of 12 regions during DJF and SON are observed in Western North America (Remer et
691 al., 2008). Specifically, in the Western region, there is a consistent increasing trend during MAM
692 ($0.004/10a$) from 1980 to 2021, while JJA and SON also show an increase after 2000, except for
693 DJF ($-0.0032/10a$). In contrast, the AOD trends in the Eastern region remain unchanged during the
694 period 1980-2021, except for MAM, which shows a stable increasing trend ($0.0033/10a$), while DJF,
695 JJA, and SON exhibit decreasing trends ($-0.0023/10a$, $-0.004/10a$, $-0.0053/10a$, respectively). In the
696 Western region, the annual mean AOD started to increase after 2005, while in the Eastern region,
697 the increase was not significant. The upward trend may be due to low rainfall and increased wildfire
698 activities (Yoon et al., 2014). The decrease in AOD in Eastern North America is related to the
699 reduction of sulfate and organic aerosols, as well as the decrease in anthropogenic emissions caused
700 by environmental regulations (Mehta et al., 2016).

701 Central South America is a relatively high aerosol loading region, sourced from biomass burning,
702 especially in SON (Remer et al., 2008; Mehta et al., 2016), with a multi-year average AOD of
703 0.192 ± 0.017 . There is a clear downward trend ($-0.01/10a$) from 1980 to 2021, which is slightly
704 greater than the trend ($0.009/10a$) from 1998 to 2010 (Hsu et al., 2012) and AOD decreased from
705 1980 to 2006 (Streets et al., 2009) and from 2001 to 2014 (Mehta et al., 2016). Although DJF (0.199)
706 and SON (0.226) have higher values compared to MAM (0.18) and JJA (0.163), the large declining
707 trends are observed in MAM ($-0.0126/10a$) and JJA ($-0.0167/10a$). It indicates that although AOD
708 has decreased overall, the aerosol loading caused by seasonal deforestation and biomass combustion
709 is still large (Mehta et al., 2016).

710 Africa is also one of the regions with a high aerosol loading worldwide. In West Africa, the average
711 AOD is 0.275 ± 0.0116 during 1980-2021, and the annual AOD shows a downward trend ($-$
712 $0.0008/10a$, $p>0.05$). The world's largest desert (Sahara Desert) is in West Africa, with much dust
713 aerosol discharged. AOD values in all seasons are above 0.25, with JJA (0.301) and MAM (0.3)
714 reaching 0.3, and DJF and SON being 0.252 and 0.25 respectively. In addition to the dust source,
715 frequent forest fires and biomass burning result in high AOD in JJA (Tian et al., 2023). The AOD
716 in DJF ($-0.0135/10a$, $p<0.01$) and SON ($-0.0026/10a$, $p>0.05$) exhibit decreasing trends, while JJA
717 ($0.0088/10a$, $p<0.01$) and MAM ($0.0037/10a$, $p>0.05$) show an opposite trend. The multi-year
718 average AOD in South Africa is 0.177 ± 0.02 , lower than that of West Africa. The annual mean AOD
719 in South Africa shows a significant decrease ($-0.0096/10a$). The AOD values range from 0.12 to 0.2
720 during 2000-2009, dominated by fine particle matter from industrial pollution from biomass and
721 fossil fuel combustion (Hersey et al., 2015). The average AOD values in DJF, MAM, JJA, and SON
722 are 0.189, 0.162, 0.147, and 0.21, respectively. JJA ($-0.0268/10a$, $p<0.01$), MAM ($-0.0126/10a$,
723 $p<0.01$) and SON ($-0.0001/10a$, $p>0.05$) exhibit a downward AOD trend, while DJF ($0.0006/10a$,



724 $p > 0.05$) shows an upward trend. AERONET and simulation results also show a decreasing trend of
725 AOD (Chin et al., 2014).

726 Australia is a region with a low aerosol loading. The multi-year mean AOD is 0.127 ± 0.014 during
727 1980-2021. The AOD ranges from 0.05 to 0.15 from AERONET during 2000-2021 and wildfires
728 are an important contributor to the aerosol loading (Yang et al., 2021a). There is a downward trend
729 of AOD ($-0.0081/10a$, $p < 0.01$), which may be related to a decrease in BC and OC (Yoon et al., 2016).
730 In addition, research has shown that the forest area in Australia has increased sharply since 2000
731 (Giglio et al., 2013), surpassing the forest fire area of the past 14 years. The seasonal average of
732 AOD in MAM, JJA, SON, and DJF are 0.122, 0.108, 0.125, and 0.151. The AOD in JJA is the
733 lowest among all seasons and regions. The highest AOD is in DJF with an increasing trend
734 ($0.0056/10a$, $p < 0.01$), while the trends during MAM, JJA and SON are $-0.0096/10a$ ($p < 0.01$), $-$
735 $0.0231/10a$ ($p < 0.01$) and $-0.0042/10a$ ($p < 0.01$), respectively. Ground-based and satellite
736 observations indicate that wildfires, biomass burning and sandstorms lead to high AOD in DJF and
737 SON. The low AOD of MAM and JJA is due to a decrease in the frequency of sandstorms and
738 wildfires and an increase in precipitation (Gras et al., 1999; Yang et al., 2021a; Yang et al., 2021b).

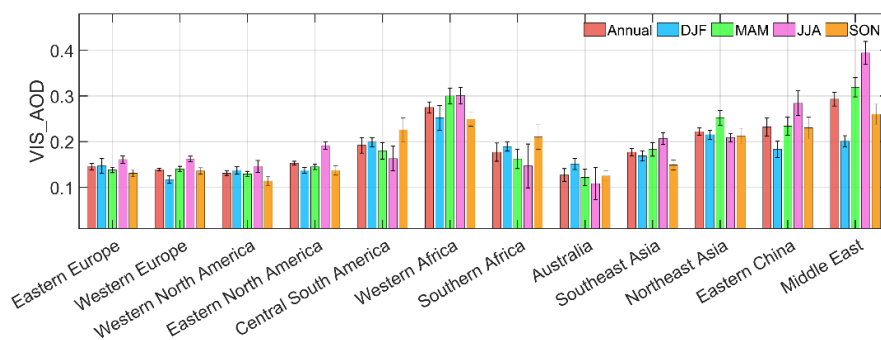
739 Asia is also a high aerosol loading area with various sources. In Southeast Asia, the multi-year
740 average AOD is 0.177 during 1980-2021 with a downward trend of AOD ($-0.0003/10a$, $p > 0.05$). It
741 is also a biomass-burning area. The seasonal average AOD ranking from high to low is JJA (0.207) >
742 MAM (0.183) > DJF (0.169) > SON (0.149). The trends in DJF ($-0.0035/10a$, $p < 0.05$), JJA ($-$
743 $0.0007/10a$, $p > 0.05$) and SON ($-0.0021/10a$, $p > 0.05$) are opposite to MAM ($0.005/10a$, $p < 0.01$).
744 Natural emissions were predominant in 1992 and 1997, because of the volcanic eruptions and forest
745 fires. Southeast Asia has no clear long-term trend in estimated AOD or observed surface solar
746 radiation (Streets et al., 2009). In Northeast Asia, the multi-year average AOD is 0.222 during 1980-
747 2021, with no significant temporal trend. The seasonal AOD values are 0.252 in MAM, 0.215 in
748 DJF, 0.212 in SON and 0.209 in JJA. AOD in MAM is significantly higher than other seasons, which
749 may be related to sandstorms in East Asia, and the reason for the high AOD in winter may be related
750 to the low boundary layer height. The trends of AOD in DJF ($-0.0025/10a$, $p > 0.05$), MAM
751 ($0.0031/10a$, $p > 0.05$), JJA (0) and SON ($-0.0006/10a$, $p > 0.05$) are not significant. In Eastern China,
752 the multi-year average AOD is 0.233, with an increasing trend ($0.0071/10a$, $p < 0.01$). The seasonal
753 average AOD ranking from high to low is JJA (0.284), MAM (0.234), SON (0.23) and DJF (0.183).
754 The AOD trends in DJF ($0.0093/10a$, $p < 0.01$), MAM ($0.0092/10a$, $p < 0.01$), JJA ($0.0038/10a$, $p > 0.05$)
755 and SON ($0.0065/10a$, $p < 0.05$) are all positive but the trend in JJA does not pass the significance
756 test. We can see that there are three stages of changes in AOD: 1980-2005, 2006-2013 and 2014-
757 2021. In the first stage, AOD increased steadily. In the second stage, AOD maintained a high level
758 of volatility. The third stage experienced a rapid decline, reaching the level of the 1980s by 2021.
759 The increasing trend of AOD before 2006 may be due to the significant increase in industrial activity,
760 and after 2013, the significant decrease is closely related to the implementation of air quality-related
761 laws and regulations, along with adjustments in the energy structure (Hu et al., 2018; Cherian &
762 Quaas, 2020).

763 In the Middle East, aerosols are influenced by local deserts and aerosols transport from Africa and
764 petroleum-related industries, resulting in high aerosol loading (Wei et al., 2019a; Wei et al., 2019b).
765 The multi-year average AOD is 0.293, which is the highest among all 12 study regions, with an
766 upward trend ($0.0027/10a$, $p > 0.05$). The aerosol loading was higher during 1980-1990 and 2000-



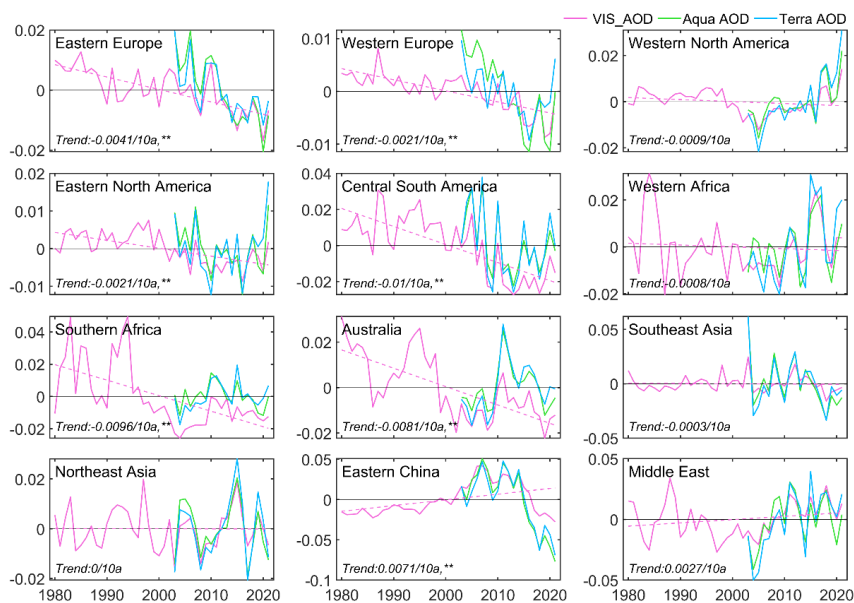
767 2021 and lower during 1990-2000. The seasonal average AOD values are 0.201 in DJF, 0.319 in
768 MAM, 0.394 in JJA, and 0.26 in SON. The trends of AOD in DJF ($-0.0039/10a$, $p<0.05$) and SON
769 ($-0.0012/10a$, $p>0.05$) show an upward trend, while the trends in MAM ($0.0067/10a$, $p<0.05$) and
770 JJA ($0.0095/10a$, $p<0.01$) are opposite. This increasing trend is related to sand and dust emissions
771 (Klingmüller et al., 2016).

772 To summarize, there are significant differences in the spatial distribution, annual trends, and
773 seasonal trends of AOD across different regions from 1980 to 201. The high aerosol loadings from
774 1980 to 2021 are in West Africa, Middle East and Asia, and low aerosol loading regions are in
775 Europe, Western North America, and Australia. Eastern China and Middle East show an increasing
776 trend, Southeast Asia and Northeast Asia show no significant trend, and the other regions show
777 downward trends. However, not all regional seasonal trends are consistent with their annual trends.
778 The results in this study have supplemented the long-term trend and distribution of AOD over land.



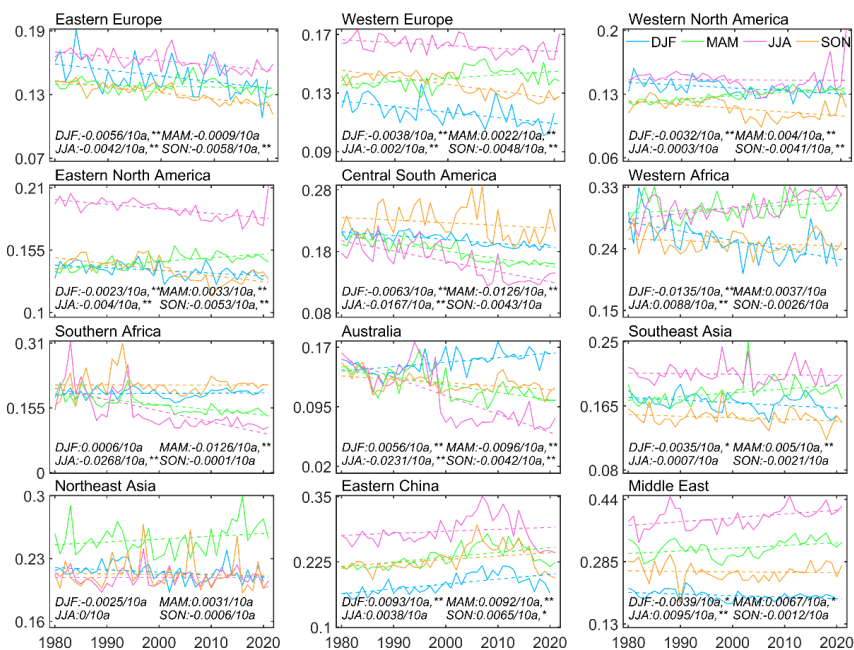
779

780 **Figure 11** Annual and seasonal averages of AOD in 12 regions during 1980-2021.



781

782 **Figure 12** Annual averages of monthly anomaly gridded VIS_AOD (pink line), Aqua (green line),
 783 and Terra (blue line) MODIS AOD in 12 regions. The dotted line is the trend line. VIS_AOD has
 784 good temporal consistency with Aqua and Terra MODIS AOD from 2003 to 2021.



785



786 **Figure 13** Seasonal averages of gridded VIS_AOD during 1980 to 2021 in 12 regions (Eastern
787 Europe, Western Europe, Western North America, Eastern North America, Central South America,
788 Western Africa, Southern Africa, Australia, Southeast Asia, Northeast Asia, Eastern China, and
789 Middle East). The dotted line is the trend line.

790 **4 Data availability**

791 The visibility-derived AOD at station and grid scales over global land from 1980 to 2021 are
792 available at National Tibetan Plateau / Third Pole Environment Data Center
793 (<https://doi.org/10.11888/Atmos.tpdc.300822>) (Hao et al., 2023).

794 **5 Conclusions**

795 In this study, we employed a machine learning technique to derive AOD for over 5000 land stations
796 worldwide, based on satellite data, visibility, and related parameters. Monthly AOD was interpolated
797 onto a 0.5° grid using ordinary kriging with area weighting. The method was trained with Aqua
798 MODIS AOD. The accuracy and performance of the derived AOD were assessed and validated
799 against Terra MODIS AOD as well as AERONET ground-based observations of AOD for the
800 corresponding stations. Evaluation of the gridded AOD was conducted using Aqua and Terra
801 MODIS AOD. We obtained daily AOD for global land stations from 1980 to 2021, as well as
802 monthly gridded AOD. The two datasets complement the shortcomings of AOD in terms of time
803 scale and spatial coverage. Finally, the spatiotemporal variation in AOD was analyzed for global
804 land, the Southern Hemisphere, the Northern Hemisphere, and 12 regions in the past 42 years.
805 Several key findings have been obtained in this study as follows.

806 1. The longer the length of the training dataset is, the better the model performs. The RMSE, MAE,
807 and R values for 100% of the training data are 0.078, 0.044, and 0.75, respectively. Increasing the
808 training set length from 5% to 100% results in a 41.1% decrease in RMSE, a 50.1% decrease in
809 MAE, and a 162.3% increase in the correlation coefficient. 97% of stations have a correlation
810 coefficient above 0.7. The correlation coefficients of daily derived AOD with Aqua, Terra, and
811 AERONET are 0.799, 0.542, and 0.514, respectively. The correlation coefficients of monthly
812 derived AOD with Aqua, Terra, and AERONET are 0.936, 0.808, and 0.61, respectively. The
813 correlation coefficients of the annual derived AOD with Aqua, Terra, and AERONET are 0.976,
814 0.906, and 0.62, respectively.

815 2. The gridded AOD is highly consistent with the satellite observations. The average biases of multi-
816 year gridded AOD compared to Aqua and Terra are 3.3% and 1.9%, respectively. The spatial
817 correlation coefficients are 0.8 and 0.79. The zonal correlation coefficients are 0.997 and 0.99, and
818 the meridional correlation coefficients are 0.986 and 0.9.

819 3. From 1980 to 2021, the global, Northern Hemisphere (NH), and Southern Hemisphere (SH) AOD
820 values are 0.161 ± 0.074 , 0.158 ± 0.076 , and 0.173 ± 0.059 , respectively. Trends in AOD for the
821 global, NH, and SH demonstrate a decreasing trend of $-0.0026/10a$, $-0.0018/10a$, and $-0.0059/10a$,
822 respectively ($p < 0.01$). The seasonal AOD ranking from high to low is JJA>MAM>DJF>SON over
823 the global land and in the NH, while in the SH, it is DJF>JJA>MAM>SON. The largest declining
824 trends are observed in NH summer and SH winter.



825 4. From 1980 to 2021, regions with high aerosol loadings (AOD > 0.2) were found in West Africa,
826 Northeast Asia, Eastern China, and the Middle East. Regions with moderate aerosol loadings (AOD
827 between 0.15 and 0.2) are Eastern North America, Central South America, South Africa, and
828 Southeast Asia. Eastern Europe, Western Europe, Western North America, and Australia are regions
829 with low aerosol loadings (AOD < 0.15). Except for Northeast Asia (no trend), Eastern Asia
830 (significant increasing trend), and the Middle East (insignificant increasing trend), other regions
831 show an upward trend of AOD. There are also seasonal differences of AOD among regions,
832 generally consistent with the seasonal variations in the NH or in the SH.

833 **Competing interests**

834 The contact author has declared that none of the authors has any competing interests.

835 **Acknowledgments**

836 This work was supported by the National Key Research & Development Program of China
837 (2022YFF0801302) and the National Natural Science Foundation of China (41930970). The hourly
838 visibility data were download from <https://mesonet.agron.iastate.edu/ASOS/>. The Aerosol Robotic
839 Network (AERONET) daily aerosol optical depth (AOD) data were download from which can be
840 downloaded from <https://aeronet.gsfc.nasa.gov>. The MODIS AOD data were download from
841 <https://ladsweb.modaps.eosdis.nasa.gov/>.

842

843 **References**

- 844 Ackerman, A. S., Hobbs, P. V., & Toon, O. B. (1995). A model for particle microphysics, turbulent mixing,
845 and radiative transfer in the stratocumulus-topped marine boundary layer and comparisons with
846 measurements. *Journal of Atmospheric Sciences*, 52(8), 1204-1236.
- 847 Albrecht, B. A. (1989). Aerosols, cloud microphysics, and fractional cloudiness. *Science*, 245(4923),
848 1227-1230.
- 849 Anderson, T. L., Charlson, R. J., Bellouin, N., Boucher, O., Chin, M., Christopher, S. A., Haywood, J.,
850 Kaufman, Y. J., Kinne, S., Ogren, J. A., Remer, L. A., Takemura, T., Tanre, D., Torres, O., Trepte,
851 C. R., Wielicki, B. A., Winker, D. M., & Yu, H. B. (2005). An "A-Train" strategy for quantifying
852 direct climate forcing by anthropogenic aerosols. *Bulletin of the American Meteorological*
853 *Society*, 86(12), 1795-+.
- 854 Andersson, S. M., Martinsson, B. G., Vernier, J.-P., Friberg, J., Brenninkmeijer, C. A., Hermann, M., Van
855 Velthoven, P. F., & Zahn, A. (2015). Significant radiative impact of volcanic aerosol in the
856 lowermost stratosphere. *Nature Communications*, 6(1), 7692.
- 857 Andrews, E., Sheridan, P. J., Ogren, J. A., Hageman, D., Jefferson, A., Wendell, J., Alástuey, A., Alados-
858 Arboledas, L., Bergin, M., & Ealo, M. (2019). Overview of the NOAA/ESRL federated aerosol
859 network. *Bulletin of the American Meteorological Society*, 100(1), 123-135.
- 860 Barnaba, F., Angelini, F., Curci, G., & Gobbi, G. P. (2011). An important fingerprint of wildfires on the
861 European aerosol load. *Atmospheric Chemistry and Physics*, 11(20), 10487-10501.
- 862 Bergstrom, R. W., Pilewskie, P., Russell, P. B., Redemann, J., Bond, T. C., Quinn, P. K., & Sierau, B.



- 863 (2007). Spectral absorption properties of atmospheric aerosols. *Atmospheric Chemistry and*
864 *Physics*, 7(23), 5937-5943.
- 865 Bescond, A., Yon, J., Girasole, T., Jouen, C., Rozé, C., & Coppalle, A. (2013). Numerical investigation
866 of the possibility to determine the primary particle size of fractal aggregates by measuring light
867 depolarization. *Journal of Quantitative Spectroscopy and Radiative Transfer*, 126, 130-139.
- 868 Boers, R., van Weele, M., van Meijgaard, E., Savenije, M., Siebesma, A. P., Bosveld, F., & Stammes, P.
869 (2015). Observations and projections of visibility and aerosol optical thickness (1956-2100) in
870 the Netherlands: impacts of time-varying aerosol composition and hygroscopicity.
871 *Environmental Research Letters*, 10(1).
- 872 Bokoye, A. I., Royer, A., O'Neil, N., Cliche, P., Fedosejevs, G., Teillet, P., & McArthur, L. (2001).
873 Characterization of atmospheric aerosols across Canada from a ground-based sunphotometer
874 network: AEROCAN. *Atmosphere-Ocean*, 39(4), 429-456.
- 875 Bösenberg, J., & Matthias, V. (2003). EARLINET: A European Aerosol Research Lidar Network to
876 Establish an Aerosol Climatology. *Max Planck Institut Fur Meteorologie*.
- 877 Bright, J. M., & Gueymard, C. A. (2019). Climate-specific and global validation of MODIS Aqua and
878 Terra aerosol optical depth at 452 AERONET stations. *Solar Energy*, 183, 594-605.
- 879 Browne, M. W. (2000). Cross-validation methods. *Journal of Mathematical Psychology*, 44(1), 108-132.
- 880 Calvo, A. I., Alves, C., Castro, A., Pont, V., Vicente, A. M., & Fraile, R. (2013). Research on aerosol
881 sources and chemical composition: Past, current and emerging issues. *Atmospheric Research*,
882 120, 1-28.
- 883 Chafe, Z. A., Brauer, M., Klimont, Z., Van Dingenen, R., Mehta, S., Rao, S., Riahi, K., Dentener, F., &
884 Smith, K. R. (2014). Household Cooking with Solid Fuels Contributes to Ambient PM_{2.5} Air
885 Pollution and the Burden of Disease. *Environmental Health Perspectives*, 122(12), 1314-1320.
- 886 Chazette, P., David, C., Lefrère, J., Godin, S., Pelon, J., & Mégie, G. (1995). Comparative lidar study of
887 the optical, geometrical, and dynamical properties of stratospheric post-volcanic aerosols,
888 following the eruptions of El Chichon and Mount Pinatubo. *Journal of Geophysical Research:*
889 *Atmospheres*, 100(D11), 23195-23207.
- 890 Che, H., Xia, X., Zhu, J., Li, Z., Dubovik, O., Holben, B., Goloub, P., Chen, H., Estelles, V., Cuevas-
891 Agullo, E., Blarel, L., Wang, H., Zhao, H., Zhang, X., Wang, Y., Sun, J., Tao, R., Zhang, X., &
892 Shi, G. (2014). Column aerosol optical properties and aerosol radiative forcing during a serious
893 haze-fog month over North China Plain in 2013 based on ground-based sunphotometer
894 measurements. *Atmospheric Chemistry and Physics*, 14(4), 2125-2138.
- 895 Che, H., Zhang, X., Chen, H., Damiri, B., Goloub, P., Li, Z., Zhang, X., Wei, Y., Zhou, H., Dong, F., Li,
896 D., & Zhou, T. (2009). Instrument calibration and aerosol optical depth validation of the China
897 Aerosol Remote Sensing Network. *Journal of Geophysical Research-Atmospheres*, 114.
- 898 Chen, A., Zhao, C., & Fan, T. (2022). Spatio-temporal distribution of aerosol direct radiative forcing over
899 mid-latitude regions in north hemisphere estimated from satellite observations. *Atmospheric*
900 *Research*, 266.
- 901 Chen, D., Ou, T., Gong, L., Xu, C.-Y., Li, W., Ho, C.-H., & Qian, W. (2010). Spatial Interpolation of
902 Daily Precipitation in China: 1951-2005. *Advances in Atmospheric Sciences*, 27(6), 1221-1232.
- 903 Cherian, R., & Quaas, J. (2020). Trends in AOD, clouds, and cloud radiative effects in satellite data and
904 CMIP5 and CMIP6 model simulations over aerosol source regions. *Geophysical Research*
905 *Letters*, 47(9), e2020GL087132.
- 906 Chin, M., Diehl, T., Tan, Q., Prospero, J., Kahn, R., Remer, L., Yu, H., Sayer, A., Bian, H., &



- 907 Geogdzhayev, I. (2014). Multi-decadal aerosol variations from 1980 to 2009: a perspective from
908 observations and a global model. *Atmospheric Chemistry and Physics*, 14(7), 3657-3690.
- 909 Chu, D., Kaufman, Y., Ichoku, C., Remer, L., Tanré, D., & Holben, B. (2002). Validation of MODIS
910 aerosol optical depth retrieval over land. *Geophysical Research Letters*, 29(12), MOD2-1-
911 MOD2-4.
- 912 Chuang, P.-J., & Huang, P.-Y. (2023). B-VAE: a new dataset balancing approach using batched
913 Variational AutoEncoders to enhance network intrusion detection. *Journal of Supercomputing*.
- 914 Deuzé, J., Goloub, P., Herman, M., Marchand, A., Perry, G., Susana, S., & Tanré, D. (2000). Estimate of
915 the aerosol properties over the ocean with POLDER. *Journal of Geophysical Research:
916 Atmospheres*, 105(D12), 15329-15346.
- 917 Dhanya, R., Paul, I. R., Akula, S. S., Sivakumar, M., & Nair, J. J. (2020). F-test feature selection in
918 Stacking ensemble model for breast cancer prediction. *Procedia Computer Science*, 171, 1561-
919 1570.
- 920 Diner, D. J., Beckert, J. C., Reilly, T. H., Bruegge, C. J., Conel, J. E., Kahn, R. A., Martonchik, J. V.,
921 Ackerman, T. P., Davies, R., & Gerstl, S. A. W. (1998). Multi-angle Imaging SpectroRadiometer
922 (MISR) instrument description and experiment overview. *IEEE Transactions on Geoscience &
923 Remote Sensing*, 98(4), 1072-1087.
- 924 Dong, Y., Li, J., Yan, X., Li, C., Jiang, Z., Xiong, C., Chang, L., Zhang, L., Ying, T., & Zhang, Z. (2023).
925 Retrieval of aerosol single scattering albedo using joint satellite and surface visibility
926 measurements. *Remote Sensing of Environment*, 294, 113654.
- 927 Dover, J., Winans, L. J., & Ams, A. M. S. (2002). *Evaluation of windshields for use in the Automated
928 Surface Observing System (ASOS)*. Paper presented at the 6th Symposium on Integrated
929 Observing Systems, Orlando, FL.
- 930 Dubovik, Oleg, Holben, Brent, Eck, Thomas, F., Smirnov, Alexander, & Kaufman (2002a). Variability
931 of Absorption and Optical Properties of Key Aerosol Types Observed in Worldwide Locations.
932 *Journal of the Atmospheric Sciences*, 59(3), 590-590.
- 933 Dubovik, O., Holben, B., Eck, T. F., Smirnov, A., Kaufman, Y. J., King, M. D., Tanré, D., & Slutsker, I.
934 (2002b). Variability of absorption and optical properties of key aerosol types observed in
935 worldwide locations. *Journal of the Atmospheric Sciences*, 59(3), 590-608.
- 936 Dubovik, O., Smirnov, A., Holben, B. N., King, M. D., Kaufman, Y. J., Eck, T. F., & Slutsker, I. (2000).
937 Accuracy assessments of aerosol optical properties retrieved from Aerosol Robotic Network
938 (AERONET) Sun and sky radiance measurements. *Journal of Geophysical Research-
939 Atmospheres*, 105(D8), 9791-9806.
- 940 Elterman, L. (1970). Relationships between vertical attenuation and surface meteorological range.
941 *Applied Optics*, 9(8), 1804-1810.
- 942 Fan, H., Zhao, C., Yang, Y., & Yang, X. (2021). Spatio-Temporal Variations of the
943 $PM_{2.5}/PM_{10}$ Ratios and Its Application to Air Pollution Type
944 Classification in China. *Frontiers in Environmental Science*, 9.
- 945 Fan, Y., & Sun, L. (2023). Satellite Aerosol Optical Depth Retrieval Based on Fully Connected Neural
946 Network (FCNN) and a Combine Algorithm of Simplified Aerosol Retrieval Algorithm and
947 Simplified and Robust Surface Reflectance Estimation (SREMARA). *IEEE Journal of Selected
948 Topics in Applied Earth Observations and Remote Sensing*.
- 949 Fernández, A., Garcia, S., Herrera, F., & Chawla, N. V. (2018). SMOTE for learning from imbalanced
950 data: progress and challenges, marking the 15-year anniversary. *Journal of artificial intelligence*



- 951 *research*, 61, 863-905.
- 952 Filonchyk, M., Yan, H., Yang, S., & Lu, X. (2018). Detection of aerosol pollution sources during
953 sandstorms in Northwestern China using remote sensed and model simulated data. *Advances in*
954 *Space Research*, 61(4), 1035-1046.
- 955 Forster, P., Ramaswamy, V., Artaxo, P., Bernsten, T., Betts, R., Fahey, D. W., Haywood, J., Lean, J., Lowe,
956 D. C., & Myhre, G. (2007). Changes in atmospheric constituents and in radiative forcing.
957 *Climate Change 2007: The Physical Science Basis. Contribution of Working Group I to the 4th*
958 *Assessment Report of the Intergovernmental Panel on Climate Change*.
- 959 Giglio, L., Randerson, J. T., & Van Der Werf, G. R. (2013). Analysis of daily, monthly, and annual burned
960 area using the fourth-generation global fire emissions database (GFED4). *Journal of*
961 *Geophysical Research: Biogeosciences*, 118(1), 317-328.
- 962 Giles, D. M., Sinyuk, A., Sorokin, M. G., Schafer, J. S., Smirnov, A., Slutsker, I., Eck, T. F., Holben, B.
963 N., Lewis, J. R., Campbell, J. R., Welton, E. J., Korkin, S. V., & Lyapustin, A. I. (2019).
964 Advancements in the Aerosol Robotic Network (AERONET) Version 3 database – automated
965 near-real-time quality control algorithm with improved cloud screening for Sun photometer
966 aerosol optical depth (AOD) measurements. *Atmos. Meas. Tech.*, 12(1), 169-209.
- 967 Goovaerts, P. (2000). Geostatistical approaches for incorporating elevation into the spatial interpolation
968 of rainfall. *Journal of Hydrology*, 228(1-2), 113-129.
- 969 Gras, J., Jensen, J., Okada, K., Ikegami, M., Zaizen, Y., & Makino, Y. (1999). Some optical properties of
970 smoke aerosol in Indonesia and tropical Australia. *Geophysical Research Letters*, 26(10), 1393-
971 1396.
- 972 Guerrero-Rascado, J. L., Landulfo, E., Antuña, J. C., Barbosa, H. d. M. J., Barja, B., Bastidas, Á. E.,
973 Bedoya, A. E., da Costa, R. F., Estevan, R., & Forno, R. (2016). Latin American Lidar Network
974 (LALINET) for aerosol research: Diagnosis on network instrumentation. *Journal of*
975 *Atmospheric and Solar-Terrestrial Physics*, 138, 112-120.
- 976 Guo, J., Zhang, J., Yang, K., Liao, H., Zhang, S., Huang, K., Lv, Y., Shao, J., Yu, T., & Tong, B. (2021).
977 Investigation of near-global daytime boundary layer height using high-resolution radiosondes:
978 first results and comparison with ERA5, MERRA-2, JRA-55, and NCEP-2 reanalyses.
979 *Atmospheric Chemistry and Physics*, 21(22), 17079-17097.
- 980 Halmer, M. M., Schmincke, H.-U., & Graf, H.-F. (2002). The annual volcanic gas input into the
981 atmosphere, in particular into the stratosphere: a global data set for the past 100 years. *Journal*
982 *of Volcanology and Geothermal Research*, 115(3-4), 511-528.
- 983 Hao, H., Wang, K., & Wu, G. (2023). *Visibility-derived aerosol optical depth over global land (1980-*
984 *2021)*. Retrieved from: <https://dx.doi.org/10.11888/Atmos.tpdc.300822>
- 985 He, H., Bai, Y., Garcia, E. A., & Li, S. (2008). *ADASYN: Adaptive synthetic sampling approach for*
986 *imbalanced learning*. Paper presented at the 2008 IEEE international joint conference on neural
987 networks (IEEE world congress on computational intelligence).
- 988 Herich, H., Kammermann, L., Gysel, M., Weingartner, E., Baltensperger, U., Lohmann, U., & Cziczo, D.
989 J. (2008). In situ determination of atmospheric aerosol composition as a function of hygroscopic
990 growth. *Journal of Geophysical Research: Atmospheres*, 113(D16).
- 991 Hersbach, H., Bell, B., Berrisford, P., Hirahara, S., Horányi, A., Muñoz-Sabater, J., Nicolas, J., Peubey,
992 C., Radu, R., & Schepers, D. (2020). The ERA5 global reanalysis. *Quarterly Journal of the*
993 *Royal Meteorological Society*, 146(730), 1999-2049.
- 994 Hersey, S. P., Garland, R. M., Crosbie, E., Shingler, T., Sorooshian, A., Piketh, S., & Burger, R. (2015).



- 995 An overview of regional and local characteristics of aerosols in South Africa using satellite,
996 ground, and modeling data. *Atmospheric Chemistry and Physics*, 15(8), 4259-4278.
- 997 Hirono, M., & Shibata, T. (1983). Enormous increase of stratospheric aerosols over Fukuoka due to
998 volcanic eruption of El Chichon in 1982. *Geophysical Research Letters*, 10(2), 152-154.
- 999 Hofmann, D., Barnes, J., O'Neill, M., Trudeau, M., & Neely, R. (2009). Increase in background
1000 stratospheric aerosol observed with lidar at Mauna Loa Observatory and Boulder, Colorado.
1001 *Geophysical Research Letters*, 36(15).
- 1002 Holben, B. N., Eck, T. F., Slutsker, I., Tanre, D., Buis, J. P., Setzer, A., Vermote, E., Reagan, J. A.,
1003 Kaufman, Y. J., Nakajima, T., Lavenu, F., Jankowiak, I., & Smirnov, A. (1998). AERONET - A
1004 federated instrument network and data archive for aerosol characterization. *Remote Sensing of
1005 Environment*, 66(1), 1-16.
- 1006 Hsu, N., Gautam, R., Sayer, A., Bettenhausen, C., Li, C., Jeong, M., Tsay, S.-C., & Holben, B. (2012).
1007 Global and regional trends of aerosol optical depth over land and ocean using SeaWiFS
1008 measurements from 1997 to 2010. *Atmospheric Chemistry and Physics*, 12(17), 8037-8053.
- 1009 Hsu, N., Jeong, M. J., Bettenhausen, C., Sayer, A., Hansell, R., Seftor, C., Huang, J., & Tsay, S. C. (2013).
1010 Enhanced Deep Blue aerosol retrieval algorithm: The second generation. *Journal of
1011 Geophysical Research: Atmospheres*, 118(16), 9296-9315.
- 1012 Hsu, N., Lee, J., Sayer, A., Carletta, N., Chen, S. H., Tucker, C., Holben, B., & Tsay, S. C. (2017).
1013 Retrieving near-global aerosol loading over land and ocean from AVHRR. *Journal of
1014 Geophysical Research: Atmospheres*, 122(18), 9968-9989.
- 1015 Hsu, N. C., Tsay, S.-C., King, M. D., & Herman, J. R. (2006). Deep blue retrievals of Asian aerosol
1016 properties during ACE-Asia. *Ieee Transactions on Geoscience and Remote Sensing*, 44(11),
1017 3180-3195.
- 1018 Hu, B., Zhang, X., Sun, R., & Zhu, X. (2019). Retrieval of Horizontal Visibility Using MODIS Data: A
1019 Deep Learning Approach. *Atmosphere*, 10(12).
- 1020 Hu, K., Kumar, K. R., Kang, N., Boiyo, R., & Wu, J. (2018). Spatiotemporal characteristics of aerosols
1021 and their trends over mainland China with the recent Collection 6 MODIS and OMI satellite
1022 datasets. *Environmental Science and Pollution Research*, 25, 6909-6927.
- 1023 Husar, R. B., Husar, J. D., & Martin, L. (2000). Distribution of continental surface aerosol extinction
1024 based on visual range data. *Atmospheric Environment*, 34(29-30), 5067-5078.
- 1025 IPCC (2021). *Climate Change 2021: The Physical Science Basis*, Cambridge University Press, New York.
- 1026 Ivanova, G., Ivanov, V., Kukavskaya, E., & Soja, A. (2010). The frequency of forest fires in Scots pine
1027 stands of Tuva, Russia. *Environmental Research Letters*, 5(1), 015002.
- 1028 Kang, Y., Choi, H., Im, J., Park, S., Shin, M., Song, C.-K., & Kim, S. (2021). Estimation of surface-level
1029 NO₂ and O₃ concentrations using TROPOMI data and machine learning over East Asia.
1030 *Environmental Pollution*, 288, 117711.
- 1031 Kang, Y., Kim, M., Kang, E., Cho, D., & Im, J. (2022). Improved retrievals of aerosol optical depth and
1032 fine mode fraction from GOCI geostationary satellite data using machine learning over East
1033 Asia. *ISPRS Journal of Photogrammetry and Remote Sensing*, 183, 253-268.
- 1034 Karbowska, B., & Zembruski, W. (2016). Fractionation and mobility of thallium in volcanic ashes after
1035 eruption of Eyjafjallajökull (2010) in Iceland. *Bulletin of environmental contamination and
1036 toxicology*, 97, 37-43.
- 1037 Kaufman, Y. J., & Boucher, O. (2002). A satellite view of aerosols in the climate system. *Nature*,
1038 419(6903), 215-215.



- 1039 Kim, D. H., Sohn, B. J., Nakajima, T., Takamura, T., Takemura, T., Choi, B. C., & Yoon, S. C. (2004).
1040 Aerosol optical properties over east Asia determined from ground-based sky radiation
1041 measurements. *Journal of Geophysical Research-Atmospheres*, 109(D2).
- 1042 King, M. D., Byrne, D. M., Herman, B. M., & Reagan, J. A. (1978). Aerosol Size Distributions Obtained
1043 by Inversions of Spectral Optical Depth Measurements. *Journal of the Atmospheric Sciences*,
1044 35(11).
- 1045 Klett, J. D. (1985). Lidar inversion with variable backscatter/extinction ratios. *Applied Optics*, 24(11),
1046 1638-1643.
- 1047 Klingmüller, K., Pozzer, A., Metzger, S., Stenchikov, G. L., & Lelieveld, J. (2016). Aerosol optical depth
1048 trend over the Middle East. *Atmospheric Chemistry and Physics*, 16(8), 5063-5073.
- 1049 Koelemeijer, R., Homan, C., & Matthijsen, J. (2006). Comparison of spatial and temporal variations of
1050 aerosol optical thickness and particulate matter over Europe. *Atmospheric Environment*, 40(27),
1051 5304-5315.
- 1052 Koschmieder, H. (1924). Theorie der horizontalen Sichtweite. 12, 33-55.
- 1053 Krylov, A., McCarty, J. L., Potapov, P., Loboda, T., Tyukavina, A., Turubanova, S., & Hansen, M. C.
1054 (2014). Remote sensing estimates of stand-replacement fires in Russia, 2002–2011.
1055 *Environmental Research Letters*, 9(10), 105007.
- 1056 Kulmala, M., Vehkamäki, H., Petäjä, T., Dal Maso, M., Lauri, A., Kerminen, V. M., Birmili, W., &
1057 McMurry, P. H. (2004). Formation and growth rates of ultrafine atmospheric particles: A review
1058 of observations. *Journal of Aerosol Science*, 35(2), 143-176.
- 1059 Kummu, M., De Moel, H., Salvucci, G., Viviroli, D., Ward, P. J., & Varis, O. (2016). Over the hills and
1060 further away from coast: global geospatial patterns of human and environment over the 20th–
1061 21st centuries. *Environmental Research Letters*, 11(3), 034010.
- 1062 Laj, P., Bigi, A., Rose, C., Andrews, E., Lund Myhre, C., Collaud Coen, M., Lin, Y., Wiedensohler, A.,
1063 Schulz, M., & Ogren, J. A. (2020). A global analysis of climate-relevant aerosol properties
1064 retrieved from the network of Global Atmosphere Watch (GAW) near-surface observatories.
1065 *Atmospheric Measurement Techniques*, 13(8), 4353-4392.
- 1066 Lapen, D. R., & Hayhoe, H. N. (2003). Spatial analysis of seasonal and annual temperature and
1067 precipitation normals in southern Ontario, Canada. *Journal of Great Lakes Research*, 29(4),
1068 529-544.
- 1069 Lee, L. A., Reddington, C. L., & Carslaw, K. S. (2016). On the relationship between aerosol model
1070 uncertainty and radiative forcing uncertainty. *Proceedings of the National Academy of Sciences*,
1071 113(21), 5820-5827.
- 1072 Levy, R. C., Mattoo, S., Munchak, L. A., Remer, L. A., Sayer, A. M., Patadia, F., & Hsu, N. C. (2013).
1073 The Collection 6 MODIS aerosol products over land and ocean. *Atmospheric Measurement
1074 Techniques*, 6(11), 2989-3034.
- 1075 Levy, R. C., Remer, L. A., Mattoo, S., Vermote, E. F., & Kaufman, Y. J. (2007). Second-generation
1076 operational algorithm: Retrieval of aerosol properties over land from inversion of Moderate
1077 Resolution Imaging Spectroradiometer spectral reflectance. *Journal of Geophysical Research:
1078 Atmospheres*, 112(D13).
- 1079 Li, J., Carlson, B. E., Yung, Y. L., Lv, D., Hansen, J., Penner, J. E., Liao, H., Ramaswamy, V., Kahn, R.
1080 A., Zhang, P., Dubovik, O., Ding, A., Lacis, A. A., Zhang, L., & Dong, Y. (2022). Scattering and
1081 absorbing aerosols in the climate system. *Nature Reviews Earth & Environment*, 3(6), 363-379.
- 1082 Li, J., Garshick, E., Hart, J. E., Li, L., Shi, L., Al-Hemoud, A., Huang, S., & Koutrakis, P. (2021).



- 1083 Estimation of ambient PM_{2.5} in Iraq and Kuwait from 2001 to 2018 using machine learning
1084 and remote sensing. *Environment International*, 151.
- 1085 Li, L. (2020). A robust deep learning approach for spatiotemporal estimation of satellite AOD and PM_{2.5}.
1086 *Remote Sensing*, 12(2), 264.
- 1087 Li, Z., Lau, W. M., Ramanathan, V., Wu, G., Ding, Y., Manoj, M., Liu, J., Qian, Y., Li, J., & Zhou, T.
1088 (2016). Aerosol and monsoon climate interactions over Asia. *Reviews of Geophysics*, 54(4),
1089 866-929.
- 1090 Lin, J. T., van Donkelaar, A., Xin, J. Y., Che, H. Z., & Wang, Y. S. (2014). Clear-sky aerosol optical depth
1091 over East China estimated from visibility measurements and chemical transport modeling.
1092 *Atmospheric Environment*, 95, 258-267.
- 1093 Liu, B., Ma, X., Ma, Y., Li, H., Jin, S., Fan, R., & Gong, W. (2022). The relationship between atmospheric
1094 boundary layer and temperature inversion layer and their aerosol capture capabilities.
1095 *Atmospheric Research*, 271.
- 1096 Mahowald, N. M., Ballantine, J. A., Feddema, J., & Ramankutty, N. (2007). Global trends in visibility:
1097 implications for dust sources. *Atmospheric Chemistry and Physics*, 7(12), 3309-3339.
- 1098 Marengo, F., Santacesaria, V., Bais, A. F., Balis, D., di Sarra, A., Papayannis, A., & Zerefos, C. (1997).
1099 Optical properties of tropospheric aerosols determined by lidar and spectrophotometric
1100 measurements (Photochemical Activity and Solar Ultraviolet Radiation campaign). *Applied*
1101 *Optics*, 36(27), 6875-6886.
- 1102 McNeill, V. F. (2017). Atmospheric Aerosols: Clouds, Chemistry, and Climate. In J. M. Prausnitz (Ed.),
1103 *Annual Review of Chemical and Biomolecular Engineering, Vol 8* (Vol. 8, pp. 427-444).
- 1104 Mehta, M., Singh, R., Singh, A., & Singh, N. (2016). Recent global aerosol optical depth variations and
1105 trends—A comparative study using MODIS and MISR level 3 datasets. *Remote Sensing of*
1106 *Environment*, 181, 137-150.
- 1107 Mitra, R., Bajpai, A., & Biswas, K. (2023). ADASYN-assisted machine learning for phase prediction of
1108 high entropy carbides. *Computational Materials Science*, 223.
- 1109 Mortier, A., Gliß, J., Schulz, M., Aas, W., Andrews, E., Bian, H., Chin, M., Ginoux, P., Hand, J., & Holben,
1110 B. (2020). Evaluation of climate model aerosol trends with ground-based observations over the
1111 last 2 decades—an AeroCom and CMIP6 analysis. *Atmospheric Chemistry and Physics*, 20(21),
1112 13355-13378.
- 1113 Mukkavilli, S., Prasad, A., Taylor, R., Huang, J., Mitchell, R., Troccoli, A., & Kay, M. (2019).
1114 Assessment of atmospheric aerosols from two reanalysis products over Australia. *Atmospheric*
1115 *Research*, 215, 149-164.
- 1116 Nagaraja Rao, C., Stowe, L., & McClain, E. (1989). Remote sensing of aerosols over the oceans using
1117 AVHRR data Theory, practice and applications. *International Journal of Remote Sensing*, 10(4-
1118 5), 743-749.
- 1119 Nakajima, T., Campanelli, M., Che, H., Estellés, V., Irie, H., Kim, S.-W., Kim, J., Liu, D., Nishizawa, T.,
1120 & Pandithurai, G. (2020). An overview of and issues with sky radiometer technology and
1121 SKYNET. *Atmospheric Measurement Techniques*, 13(8), 4195-4218.
- 1122 NOAA, DOD, FAA, & USN (1998). Automated Surface Observing System (ASOS) User's Guide.
- 1123 O'Reilly, J. E., Maritorena, S., Mitchell, B. G., Siegel, D. A., Carder, K. L., Garver, S. A., Kahru, M., &
1124 McClain, C. (1998). Ocean color chlorophyll algorithms for SeaWiFS. *Journal of Geophysical*
1125 *Research-Oceans*, 103(C11), 24937-24953.
- 1126 Pebesma, E. J. (2004). Multivariable geostatistics in S: the gstat package. *Computers & Geosciences*,



- 1127 30(7), 683-691.
- 1128 Prakash, P. J., Stenchikov, G., Kalenderski, S., Osipov, S., & Bangalath, H. (2014). The impact of dust
1129 storms on the Arabian Peninsula and the Red Sea. *Atmospheric Chemistry & Physics*
1130 *Discussions*, 14(13).
- 1131 Qiu, J. (1997). The method of wide-band remote atmospheric aerosol optical depth and its application
1132 (in Chinese). *J. Remote Sens.*, 1(1), 15-23.
- 1133 Qiu, J., & Lin, Y. (2001). A parameterization model of aerosol optical depths in China. *Acta*
1134 *Meteorologica Sinica*, 59(3), 368-372.
- 1135 Ramanathan, V., Crutzen, P. J., Kiehl, J., & Rosenfeld, D. (2001). Aerosols, climate, and the hydrological
1136 cycle. *Science*, 294(5549), 2119-2124.
- 1137 Remer, L. A., Kaufman, Y. J., Tanre, D., Mattoo, S., Chu, D. A., Martins, J. V., Li, R. R., Ichoku, C.,
1138 Levy, R. C., Kleidman, R. G., Eck, T. F., Vermote, E., & Holben, B. N. (2005). The MODIS
1139 aerosol algorithm, products, and validation. *Journal of the Atmospheric Sciences*, 62(4), 947-
1140 973.
- 1141 Remer, L. A., Kleidman, R. G., Levy, R. C., Kaufman, Y. J., Tanre, D., Mattoo, S., Martins, J. V., Ichoku,
1142 C., Koren, I., Yu, H., & Holben, B. N. (2008). Global aerosol climatology from the MODIS
1143 satellite sensors. *Journal of Geophysical Research-Atmospheres*, 113(D14).
- 1144 Salomonson, V. V., Barnes, W. L., Maymon, P. W., Montgomery, H. E., & Ostrow, H. (1987). MODIS:
1145 advanced facility instrument for studies of the Earth as a system. *Geoscience & Remote Sensing*
1146 *IEEE Transactions on*, 27(2), 145-153.
- 1147 Sawamura, P., Vernier, J. P., Barnes, J. E., Berkoff, T. A., Welton, E. J., Alados-Arboledas, L., Navas-
1148 Guzmán, F., Pappalardo, G., Mona, L., & Madonna, F. (2012). Stratospheric AOD after the 2011
1149 eruption of Nabro volcano measured by lidars over the Northern Hemisphere. *Environmental*
1150 *Research Letters*, 7(3), 34013-34021(34019).
- 1151 Singh, A., Mahata, K. S., Rupakheti, M., Junkermann, W., Panday, A. K., & Lawrence, M. G. (2019). An
1152 overview of airborne measurement in Nepal—Part 1: Vertical profile of aerosol size, number,
1153 spectral absorption, and meteorology. *Atmospheric Chemistry and Physics*, 19(1), 245-258.
- 1154 Smirnov, A., Holben, B., Slutsker, I., Giles, D., McClain, C., Eck, T., Sakerin, S., Macke, A., Croot, P.,
1155 & Zibordi, G. (2009). Maritime aerosol network as a component of aerosol robotic network.
1156 *Journal of Geophysical Research: Atmospheres*, 114(D6).
- 1157 Steinberg, D., & Colla, P. (2009). CART: classification and regression trees. *The top ten algorithms in*
1158 *data mining*, 9, 179.
- 1159 Streets, D. G., Yan, F., Chin, M., Diehl, T., Mahowald, N., Schultz, M., Wild, M., Wu, Y., & Yu, C. (2009).
1160 Anthropogenic and natural contributions to regional trends in aerosol optical depth, 1980–2006.
1161 *Journal of Geophysical Research: Atmospheres*, 114(D10).
- 1162 Sun, E., Xu, X., Che, H., Tang, Z., Gui, K., An, L., Lu, C., & Shi, G. (2019). Variation in MERRA-2
1163 aerosol optical depth and absorption aerosol optical depth over China from 1980 to 2017.
1164 *Journal of Atmospheric and Solar-Terrestrial Physics*, 186, 8-19.
- 1165 Sun, Y., & Zhao, C. (2020). Influence of Saharan dust on the large-scale meteorological environment for
1166 development of tropical cyclone over North Atlantic Ocean Basin. *Journal of Geophysical*
1167 *Research: Atmospheres*, 125(23), e2020JD033454.
- 1168 Teixeira, A. (2004). Classification and regression tree. *Revue Des Maladies Respiratoires*, 21(6), 1174-
1169 1176.
- 1170 Tian, X., Tang, C., Wu, X., Yang, J., Zhao, F., & Liu, D. (2023). The global spatial-temporal distribution



- 1171 and EOF analysis of AOD based on MODIS data during 2003-2021. *Atmospheric Environment*,
1172 302.
- 1173 Tupper, A., Oswalt, J. S., & Rosenfeld, D. (2005). Satellite and radar analysis of the volcanic-
1174 cumulonimbi at Mount Pinatubo, Philippines, 1991. *Journal of Geophysical Research:*
1175 *Atmospheres*, 110(D9).
- 1176 Vasilyev, O., Contreras, A. L., Velazquez, A. M., Fabi, R. P. y., Ivlev, L., Kovalenko, A., Vasilyev, A.,
1177 Jukov, V., & Welch, R. M. (1995). Spectral optical properties of the polluted atmosphere of
1178 Mexico City (spring-summer 1992). *Journal of Geophysical Research: Atmospheres*, 100(D12),
1179 26027-26044.
- 1180 Vernier, J. P., Thomason, L. W., Pommereau, J. P., Bourassa, A., Pelon, J., Garnier, A., Hauchecorne, A.,
1181 Blanut, L., Trepte, C., & Degenstein, D. (2011). Major influence of tropical volcanic eruptions
1182 on the stratospheric aerosol layer during the last decade. *Geophysical Research Letters*, 38(12).
- 1183 Wang, K., Dickinson, R. E., & Liang, S. (2009). Clear Sky Visibility Has Decreased over Land Globally
1184 from 1973 to 2007. *Science*, 323(5920), 1468-1470.
- 1185 Wang, K. C., Dickinson, R. E., Su, L., & Trenberth, K. E. (2012). Contrasting trends of mass and optical
1186 properties of aerosols over the Northern Hemisphere from 1992 to 2011. *Atmospheric Chemistry*
1187 *and Physics*, 12(19), 9387-9398.
- 1188 Wei, J., Li, Z., Peng, Y., & Sun, L. (2019a). MODIS Collection 6.1 aerosol optical depth products over
1189 land and ocean: validation and comparison. *Atmospheric Environment*, 201, 428-440.
- 1190 Wei, J., Peng, Y., Guo, J., & Sun, L. (2019b). Performance of MODIS Collection 6.1 Level 3 aerosol
1191 products in spatial-temporal variations over land. *Atmospheric Environment*, 206, 30-44.
- 1192 Welton, E. J., Campbell, J. R., Berkoff, T. A., Spinhirne, J. D., & Starr, D. O. (2002). The micro-pulse
1193 lidar network (MPLNET).
- 1194 Winker, D. M., Tackett, J. L., Getzewich, B. J., Liu, Z., Vaughan, M. A., & Rogers, R. R. (2013). The
1195 global 3-D distribution of tropospheric aerosols as characterized by CALIOP. *Atmospheric*
1196 *Chemistry and Physics*, 13(6), 3345-3361.
- 1197 Winker, D. M., Vaughan, M. A., Omar, A., Hu, Y., Powell, K. A., Liu, Z., Hunt, W. H., & Young, S. A.
1198 (2009). Overview of the CALIPSO Mission and CALIOP Data Processing Algorithms. *Journal*
1199 *of Atmospheric and Oceanic Technology*, 26(11), 2310-2323.
- 1200 Wu, J., Luo, J., Zhang, L., Xia, L., Zhao, D., & Tang, J. (2014). Improvement of aerosol optical depth
1201 retrieval using visibility data in China during the past 50years. *Journal of Geophysical*
1202 *Research-Atmospheres*, 119(23), 13370-13387.
- 1203 Xia, X., Che, H., Zhu, J., Chen, H., Cong, Z., Deng, X., Fan, X., Fu, Y., Goloub, P., & Jiang, H. (2016).
1204 Ground-based remote sensing of aerosol climatology in China: Aerosol optical properties, direct
1205 radiative effect and its parameterization. *Atmospheric Environment*, 124(JAN.PT.B), 243-251.
- 1206 Xie, Y., Wang, Y., Zhang, K., Dong, W., Lv, B., & Bai, Y. (2015). Daily estimation of ground-level PM_{2.5}
1207 concentrations over Beijing using 3 km resolution MODIS AOD. *Environmental Science &*
1208 *Technology*, 49(20), 12280-12288.
- 1209 Yang, X., Wang, Y., Zhao, C., Fan, H., Yang, Y., Chi, Y., Shen, L., & Yan, X. (2022). Health risk and
1210 disease burden attributable to long-term global fine-mode particles. *Chemosphere*, 287.
- 1211 Yang, X., Zhao, C., Yang, Y., & Fan, H. (2021a). Long-term multi-source data analysis about the
1212 characteristics of aerosol optical properties and types over Australia. *Atmospheric Chemistry*
1213 *and Physics*, 21(5), 3803-3825.
- 1214 Yang, X., Zhao, C., Yang, Y., Yan, X., & Fan, H. (2021b). Statistical aerosol properties associated with



- 1215 fire events from 2002 to 2019 and a case analysis in 2019 over Australia. *Atmospheric Chemistry*
1216 *and Physics*, 21(5), 3833-3853.
- 1217 Yang, Y., Ge, B., Chen, X., Yang, W., Wang, Z., Chen, H., Xu, D., Wang, J., Tan, Q., & Wang, Z. (2021c).
1218 Impact of water vapor content on visibility: Fog-haze conversion and its implications to
1219 pollution control. *Atmospheric Research*, 256.
- 1220 Yoon, J., Burrows, J., Vountas, M. v., von Hoyningen-Huene, W., Chang, D., Richter, A., & Hilboll, A.
1221 (2014). Changes in atmospheric aerosol loading retrieved from space-based measurements
1222 during the past decade. *Atmospheric Chemistry and Physics*, 14(13), 6881-6902.
- 1223 Yoon, J., Pozzer, A., Chang, D. Y., Lelieveld, J., Kim, J., Kim, M., Lee, Y., Koo, J.-H., Lee, J., & Moon,
1224 K. (2016). Trend estimates of AERONET-observed and model-simulated AOTs between 1993
1225 and 2013. *Atmospheric Environment*, 125, 33-47.
- 1226 Zhang, S., Wu, J., Fan, W., Yang, Q., & Zhao, D. (2020). Review of aerosol optical depth retrieval using
1227 visibility data. *Earth-Science Reviews*, 200, 102986.
- 1228 Zhang, Z., Wu, W., Wei, J., Song, Y., Yan, X., Zhu, L., & Wang, Q. (2017). Aerosol optical depth retrieval
1229 from visibility in China during 1973-2014. *Atmospheric Environment*, 171, 38-48.
- 1230 Zhao, A. D., Stevenson, D. S., & Bollasina, M. A. (2019). The role of anthropogenic aerosols in future
1231 precipitation extremes over the Asian Monsoon Region. *Climate Dynamics*, 52(9-10), 6257-
1232 6278.
- 1233 Ziemba, L. D., Lee Thornhill, K., Ferrare, R., Barrick, J., Beyersdorf, A. J., Chen, G., Crumeyrolle, S.
1234 N., Hair, J., Hostetler, C., & Hudgins, C. (2013). Airborne observations of aerosol extinction by
1235 in situ and remote-sensing techniques: Evaluation of particle hygroscopicity. *Geophysical*
1236 *Research Letters*, 40(2), 417-422.
- 1237